Contents lists available at ScienceDirect

Chemie der Erde

journal homepage: www.elsevier.de/chemer

INVITED REVIEW

Thermal infrared (vibrational) spectroscopy of Mg–Fe olivines: A review and applications to determining the composition of planetary surfaces

Victoria E. Hamilton*

Southwest Research Institute, 1050 Walnut Street, Suite 300, Boulder, CO 80302, USA

ARTICLE INFO

Article history:
Received 9 September 2009
Received in revised form
14 December 2009
Accepted 14 December 2009

Keywords:
Olivine
Spectroscopy
Remote sensing
Thermal infrared

ABSTRACT

The reststrahlen features in thermal infrared, or vibrational, spectra of Mg-Fe olivines ($(Mg,Fe)_2SiO_4$) exhibit trends in position, strength, and number of features that are diagnostic of the relative proportions of the Mg and Fe cations in the minerals. Although band positions move to lower wavenumbers (longer wavelengths) across the forsterite–fayalite compositional binary in a generally linear manner, specific feature shifts in transmittance data are described best by two linear fits with a break in slope near Fo_{70}. The break in slope may be accompanied by an offset as well; both traits are attributed to structural changes in olivine brought about by distortion of the crystal lattice by Fe. Reflectance and emissivity spectra exhibit similar trends in band position with composition, and all three types of data demonstrate that some olivine band strengths change across the Mg–Fe solid solution series and also are diagnostic of composition. Olivines have been identified in a wide array of thermal infrared spectra of planetary materials and have been interpreted as being present on the surfaces of Mercury, the Moon, Mars, and a number of asteroids based on the analysis of thermal infrared spectra. New linear least squares models of the emissivity spectra of olivine-bearing Martian meteorites enable a preliminary estimation of the accuracy with which quantitative estimates of olivine abundance and solid solution composition can be derived from the spectra of mixtures.

1. Introduction

Members of the olivine group ("olivines" hereafter) are important rock-forming minerals in terrestrial, planetary, and astronomical geomaterials. Olivines are the major component of Earth's mantle, they are common in many kinds of meteorites, and have been identified on the surfaces of planetary bodies, and in the spectra of astronomical targets. Olivine phases are indicators of low-silica environments, they crystallize at high temperatures, and they generally break down readily in the presence of weathering agents such as water. As such, their identification and characterization is a subject of considerable interest to a wide variety of researchers. Spectroscopy can be used very effectively in the laboratory to study the fine-scale structural properties of natural and experimentally produced olivines (e.g., as functions of temperature and pressure). Spectroscopy also can be used in remote-sensing applications to identify olivines in data acquired of non-terrestrial environments. Spectroscopic methods for examining olivines (and other minerals) generally utilize visible through infrared wavelengths, which are the wavelengths in which geologic materials have diagnostic spectral signatures.

Deer et al. (1992) provide detailed descriptions of the characteristics of olivine minerals, portions of which are summarized here. Olivines are silicate minerals with orthorhombic symmetry and having a general formula of X_2SiO_4, where X represents one or more divalent atoms in six-fold coordination with isolated silicate tetrahedra. The most common cations in olivine are Mg^{2+} and Fe^{2+}, forming a solid solution between forsterite (Mg_2SiO_4) and fayalite (Fe_2SiO_4). Compositions in the Mg–Fe series commonly are identified by the molar percentages of forsterite (Fo) and fayalite (Fa) (e.g., $Fo_{90}Fa_{10}$), or in shortened form, by just their forsterite number, where $Fo_\# = Mg/(Mg+Fe) \times 100$. In this paper, the derivation of forsterite number is modified slightly ($Fo_\# = Mg/(Mg+Fe+Ca+Mn) \times 100$) to account for other cations that may substitute into the olivine structure in small amounts, and serves to ensure that all data being compared have similarly derived $Fo_\#$. In a few cases, this formulation results in very slight absolute differences in $Fo_\#$ ($< Fo_2$) from values published by the original authors. Olivine with up to one formula unit of calcium ($CaMgSiO_4$) is referred to as monticellite. The iron analogue, kirschsteinite ($CaFeSiO_4$), is rare in nature as a pure phase, but olivine in terrestrial rocks and meteorites may contain a predominance of this molecule and it is readily synthesized. There also is a manganese end

---

* Tel.: +1 720 240 0115; fax: +1 303 546 9687.
E-mail address: hamilton@boulder.swri.edu

0009-2819/$ - see front matter
doi:10.1016/j.chemer.2009.12.005

member, tephroite (Mn_2SiO_4). The metal cations occupy two positions in the crystal structure, M1 and M2, which are defined by their symmetry; commonly, Fe^{2+} displays a preference for the M1 site. The thermal behavior of olivines along the Mg–Fe binary is such that the first olivines to crystallize from a liquid are Mg-rich relative to the compositions that crystallize subsequently. Among silicate minerals, olivines are relatively susceptible to mechanical and chemical breakdown, as well as low-grade metamorphism. Common products of these reactions are serpentine and mixtures of mostly phyllosilicates and oxides that are referred to as iddingsite, chlorophaeite, and bowlingite, depending on the mixture components. Serpentinization is the most common form of olivine alteration and can be thought of in simple terms as the hydration of olivine to yield serpentine ($Mg_3Si_2O_5(OH)_4$).

On Earth, olivine compositions in the forsterite–fayalite series are common in mafic to ultramafic rocks, in which their compositions typically range from about Fo_{85-95}. Compositions between Fo_{80} and Fo_{50} are typical of gabbroic rocks; more Fe-rich compositions are less common, occurring in ferrodiorites, mangerites, and quartz syenites. They also are present in progressively metamorphosed serpentinites and thermally metamorphosed iron-rich sediments. In addition to terrestrial occurrences, Mg–Fe olivines are constituents of stony and stony–iron meteorites, and have been identified on the surfaces of Mars and some asteroids, in comets, in interplanetary and interstellar dusts, and in the circumstellar regions around some evolved and pre-main sequence stars. Olivines are, quite literally, universally relevant minerals, and it is their identification and discrimination in planetary materials and on planetary surfaces that will be the primary emphasis here.

In this paper, I will focus on the spectral characteristics of olivines along the Mg–Fe binary in the thermal, or middle, infrared region of the electromagnetic spectrum, from ~1200 to 200 cm^{-1} (~8.3–50 μm). Spectroscopy in the thermal infrared (TIR) region also is referred to in the literature as vibrational spectroscopy because within this range, spectral features arise from the fundamental vibrational modes of the material. More specifically, crystalline solids such as minerals are composed of a regular, repeating pattern of positive and negative ions that vibrate at quantized frequencies. When the positive and negative ions move out of phase with each other, absorption of energy becomes possible at the wavelength corresponding to the vibrational frequency of the motions, as long as there is a net dipole moment. For example, in silicate minerals the primary spectral absorptions (reststrahlen bands) are due to the stretching and bending motions in the silicon–oxygen anions. Additional absorption features result from metal–oxygen and lattice vibrations. The exact frequencies, shapes, intensities, and number of features in a mineral's spectrum are dependent on the relative masses, radii, distances, and angles between atoms and their bond strengths. These parameters are determined by the structural arrangement of the anions (i.e., their polymerization), and the location and composition of the cations associated with them. Because all minerals, by definition, have unique structures and/or compositions, virtually every mineral has a different suite of vibrational absorption characteristics and thus a unique spectrum in the thermal infrared. Several spectroscopic techniques are capable of measuring the fundamental vibrational modes of minerals, including: transmission, reflection, emission, attenuated total reflection (ATR), and Raman. Of interest here are the results from transmission, reflectance, and emission spectroscopy, where transmission data have provided much of the fundamental information on olivine spectral characteristics in a variety of pure and mixed samples, and reflectance and emission spectra are currently used for determining the composition of planetary materials and surfaces (from returned samples, meteorites, and remote sensing).

The first objective of this paper (Sections 2–4) is to provide an overview of the peer-reviewed literature discussing the TIR properties of the Mg–Fe olivine series as a function of composition and physical character as measured by transmission and reflection spectroscopy, along with some new analyses of previously published data. I also will present new emission data of Mg–Fe olivine samples, where emission is the technique used for remote sensing of planetary surfaces. Additionally, I will review the literature on TIR observations of olivine in planetary materials, and the identification of Mg–Fe olivines on planetary surfaces via TIR spectroscopy. Additional discussion (Section 5) will be dedicated to describing how olivines can identified in mixture spectra and the accuracy with which their solid solution compositions and abundances can be obtained from those spectra. To my knowledge, a quantitative demonstration of the accuracy and precision with which olivine compositions and abundances can be distinguished in the emission spectra of natural mixtures has not been presented previously. The analyses of transmission, reflection, and emission data presented here complement the existing literature and will provide additional information that can aid the identification of olivines on planetary surfaces. With this application in mind, I have plotted composition and fit regressions as a function of various spectral feature parameters, rather than portraying spectral features as the dependent variable. This approach allows a consideration of how well one might expect to predict olivine composition from spectral features in remote-sensing data or when other compositional analyses are lacking for laboratory samples. Finally, I wish to point out that there are numerous un-peer-reviewed conference and workshop abstracts and papers that bear on the topic of olivine spectroscopy in the laboratory and on planetary surfaces. Because such papers do not always represent final results I have not attempted to summarize these references in this review, but I encourage interested readers to seek them out for additional information.

2. Thermal infrared spectroscopy of the Mg–Fe olivine series

2.1. *Focus of this review and definitions*

The motivations for and applications of olivine spectral studies are wide-ranging, covering fields from astronomy to mantle geophysics, and as such, a wide variety of measurement techniques and samples are found in the literature. An exhaustive review of the literature on TIR spectroscopy of olivines could fill a book, so with application to planetary surfaces in mind, the discussion here will focus on the highlights of observational spectroscopy of Mg–Fe olivines as a series and in solid planetary materials or their analogues, largely setting aside discussion of other substitution series (e.g., Duke and Stephens, 1964), and theoretical calculations of vibrational modes and corresponding experimental derivation of optical constants (e.g., Servoin and Piriou, 1973; Iishi, 1978; Hofmeister, 1997; Fabian et al., 2001). In terms of what constitutes "olivine" for the purposes of this review, a wide range of sample types have been investigated, such as natural and synthetic samples, single crystals, bulk samples, and powders.

In this review, I will focus on data collected by transmission, reflection, and emission techniques. Below I describe the nature of these measurements, excluding details of calibration, which can be examined on a case-by-case basis in the spectroscopy literature. Although Raman and attenuated total reflectance (ATR) spectroscopy are applicable to in situ planetary studies and measure the vibrational properties of geologic phases, they are sufficiently different as measurement techniques from transmission, reflection, and emission spectroscopy that they will not be discussed here. Particularly, it should be noted that not all infrared active vibrational modes are Raman active and vice versa, so infrared and Raman measurements are complementary but not directly comparable.

Fig. 1 shows spectra of quartz acquired via transmission, reflection, and emission spectroscopy (a demonstration using olivine spectra would have been preferable, but the requisite data for a common composition are not available). The positions of spectral features are shown in units of wavenumber (cm^{-1}), where dividing 10,000 by wavenumber yields wavelength in microns (μm). As not all readers may be familiar with the differences between these techniques, here I provide a brief overview. *Transmission* refers to the passing of radiant energy through a material. Transmission spectroscopy measures the quantity of infrared light transmitted through a sample (as a function of wavelength), usually a powder or thin-film mounted in or on a transparent medium such as KBr. The ratio of the measured spectrum to a reference spectrum of the transparent medium commonly is presented as relative (qualitative) or percent (quantitative) *transmittance*, where diagnostic fundamental spectral features that are indicative of highly absorbing molecular vibrations are minima (troughs). Spectra may also be presented in the inverse, as *absorbance*, where the diagnostic features of interest are maxima (peaks). Semantically, one may argue that these should be referred to as *transmissivity* or *absorptivity* spectra because the spectrum is that of a ratio, not the original measured transmittance (or absorbance), but this is not the convention in contemporary literature. *Reflection* refers to a process whereby incident light is returned from a material's surface. In reflection spectroscopy, the material of interest, typically an optically thick particulate or solid sample, is illuminated with an infrared light source; the ratio of the amount of light reflected to the amount of light incident yields a spectrum with maxima in the locations associated with molecular vibrations. Reflectance can vary with thickness, so the percentage of light reflected from an optically thick material is described most accurately as its *reflectivity*. However, in much of the spectroscopy literature such spectra are presented as percent *reflectance,* so I follow that convention here. *Emission* refers to the energy radiated from a material. Measurements of emission do not utilize an external light source, but instead passively measure the wavelength-dependent emitted infrared radiance of the sample (i.e., the sample is the source), which may be a particulate or solid. *Emissivity* is defined as the ratio of the energy emitted from a material to that of a blackbody (perfect emitter) at the same temperature and has unitless dimensions from 0 to 1. Emission is reduced at frequencies where the material is strongly absorbing and the features of interest in an emissivity spectrum are minima (emissivity is the term most commonly used in the literature and it is used here). Readers familiar with the astronomical literature may be aware that there are references to "emission peaks" observed in the infrared spectra of cometary dust, circumstellar disks, etc. Emission peaks are observed because the temperature of the dust or gas is hotter than that of the background flux. Because the dust, gas, and background are not in thermal equilibrium, such spectra cannot be called emissivity (and usually are not labeled as such).

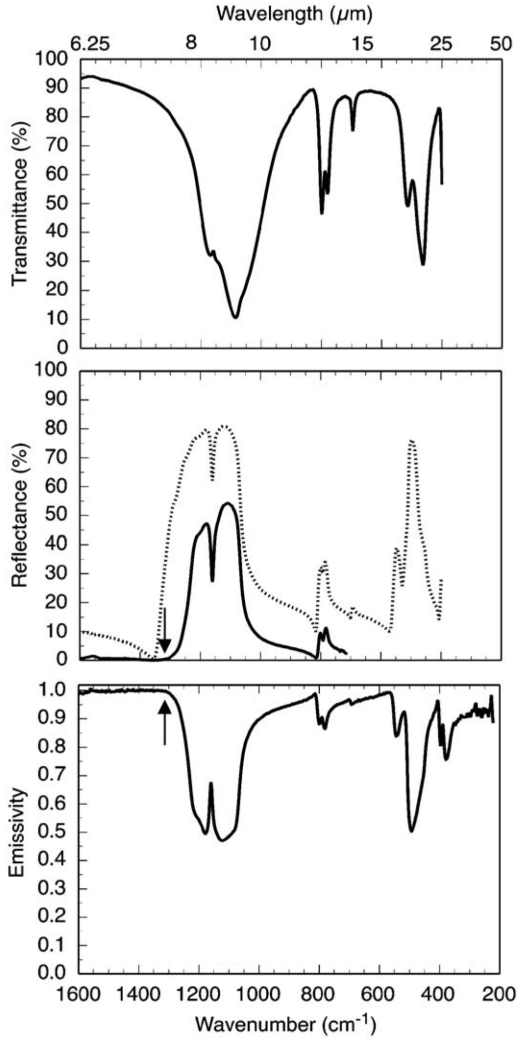

Fig. 1. Transmittance, biconical (dotted) and hemispherical (solid) reflectance, and emissivity spectra of α-quartz. Arrows denote the location of the primary Christiansen feature (CF). Transmittance and reflectance data are from Salisbury et al. (1992), emissivity data are from Christensen et al. (2000b).

Transmission spectroscopy measures only the imaginary part of the complex refractive index, whereas reflection and emission spectroscopy measure both the real and imaginary parts of the complex refractive index. As such, the positions of features determined from transmittance (or absorbance) spectra are only an approximate guide to the locations of comparable features in reflectance and emissivity spectra. Reflectance and emissivity spectra are inverses of each other (E=1–R), according to Kirchhoff's law (Nicodemus, 1965). However, this is only strictly true for cases where the reflectance spectra are measured such that the solid angle of the measurement is low enough to exclude grazing and near-grazing angles of incidence and collection. If grazing angles are included, forward scattering results in distortion of the spectrum, most notably near the Christiansen feature (CF), the reflectance minimum/emission maximum on the high wavenumber side of the fundamental molecular vibration bands (see the biconical reflectance spectrum in Fig. 1). Grazing angles may be physically blocked (Salisbury et al., 1991a) or they can be avoided by the use of an integrating sphere that permits the measurement of directional hemispherical reflectance (Fig. 1) (Salisbury et al., 1991a).

2.2. *Infrared band assignments*

Thermal infrared band assignments for Mg–Fe olivines were determined early on by Tarte (1963), Oehler and Günthard (1969), and Devarajan and Funck (1975) from transmission spectra, and many studies have resulted in refined and extended assignments since then based on transmission and polarized and unpolarized reflection spectra (e.g., see summaries by Reynard (1991) and

Please cite this article as: Hamilton, V.E., (2010), doi:10.1016/j.chemer.2009.12.005

Hofmeister (1997)). As described by Reynard (1991), symmetry analysis indicates that there are a total of 84 normal modes of vibration, 35 of which are infrared active (but which may not be individually observable in unpolarized spectra, or may be too weak to be observed). These modes represent internal stretching and bending modes as well as lattice modes (cation translations and rigid rotation–translation) of the SiO_4 tetrahedra. In spectra of randomly oriented (e.g., particulate, powder dispersed, or thin-film) samples, the three principal bands between ~1000 and 850 cm^{-1} (~10 and 11.8 μm) are the result of splitting of degenerate Si–O asymmetric stretching vibrations of the ν_3 mode in SiO_4. A feature near 825 cm^{-1} (12.1 μm) results from the ν_1 mode (symmetric stretch), and three or four features in the ~610–460 cm^{-1} (~16.4–21.7 μm) region can be attributed to splitting of the degenerate ν_4 asymmetric bending vibration. Features in the 500–200 cm^{-1} (20–50 μm) region are attributable to the ν_2 symmetric bending mode, rotations and translation of the SiO_4 tetrahedron, and translations of one of the divalent cations. In the far infrared (200–85 cm^{-1}; 50–117.6 μm), additional translational modes and combinations of SiO_4 and cation translations are observed (Hofmeister, 1997). It should be noted that in addition to the fundamental bands, other (usually weaker) bands may be observed that are attributable to combinations or overtones of fundamental features.

The vibrational modes in olivine series minerals vary slightly as a function of solid solution composition, leading to shifts in band position and changes in band strength, including the presence or absence of some features. Physical characteristics and environmental conditions also can affect the measured TIR spectrum. Details of these trends for transmission, reflectance, and emissivity spectra are described in the following sections.

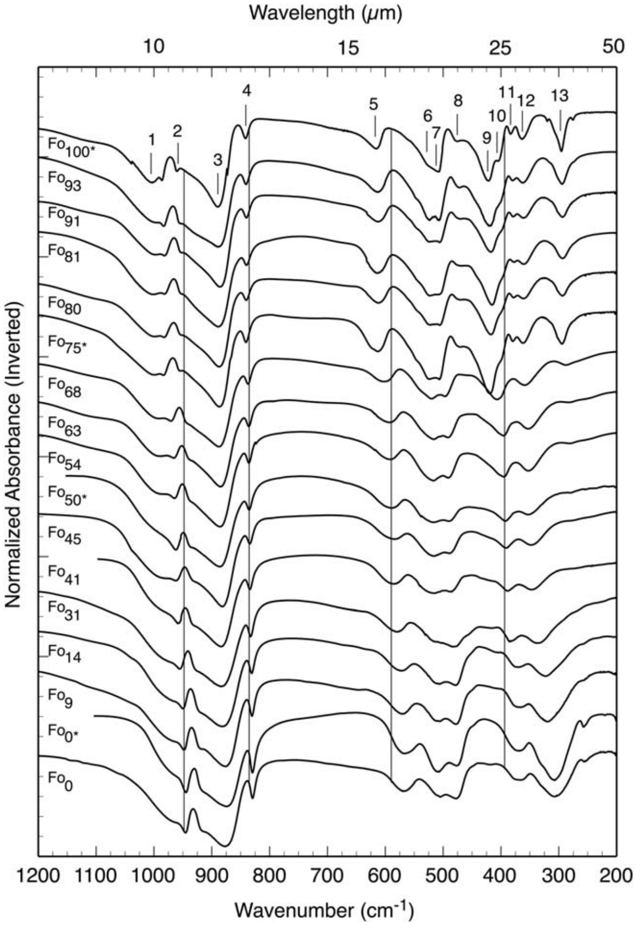

Fig. 2. Thin-film transmission spectra (offset for clarity) of 17 Mg–Fe series olivines (Hofmeister and Pitman, 2007). Band numbers are as defined by Burns and Huggins (1972). Vertical lines are for visual reference, and indicate the positions of features in the Fo$_{50}$ spectrum, from left to right: the peak between Bands 1 and 2, Band 4, Band 5, and Band 9. Asterisks denote synthetic samples.

2.3. *Transmission data—spectral trends as a function of solid solution composition*

Numerous investigators have examined in detail olivine band positions as a function of composition in transmission data (e.g., Lehmann et al., 1961; Lyon, 1962; Tarte, 1963; Duke and Stephens, 1964; Burns and Huggins, 1972; Jäger et al., 1998; Koike et al., 2003; Tarantino et al., 2003; Hofmeister and Pitman, 2007). These studies have shown that within the olivine series, there are variations in the positions and number of the absorption bands with Mg–Fe substitution. Generally, the position of each absorption band shifts systematically with the proportion of the substituent cations, although the shifts are not all linear or continuous. Fig. 2 shows an example series of Mg–Fe olivine thin-film transmittance spectra over the spectral range 1200–200 cm^{-1}, acquired by Hofmeister and Pitman (2007). (This figure and some others in this paper show normalized spectra to draw attention to the variations in band positions rather than absolute strengths. Not all measurement techniques yield directly comparable band strengths, so the reader interested in quantitative band strength characteristics is referred to the references herein, where the original data and details of the measurement approaches are described.) The band numbering scheme employed in this paper is that of Burns and Huggins (1972) and was derived by those authors based on the features observed in their forsterite (Fo$_{91}$) spectrum. Fig. 3**a** illustrates absorption band positions and trends using band positions derived from the transmission spectra of Duke and Stephens (1964), Burns and Huggins (1972), Salisbury et al. (1991b), Koike et al. (2003), and Hofmeister and Pitman (2007). These studies are among those containing the greatest number and/or range of olivine compositions with published spectra and/or band positions, and most band positions can be determined to 1 cm^{-1} in these data. Band positions plotted for the data of Duke and Stephens (1964), Burns and Huggins (1972), and Koike et al. (2003) were taken from tables in those papers. I determined band positions for data acquired by Salisbury et al. (1991b) and Hofmeister and Pitman (2007) from digital spectra available online and their values are given in Table 1. Data for bands 6, 8, 10, 11, and 13 are not shown in band position figures in this review because these features are not always present in transmittance, reflectance, and emissivity spectra of the full compositional range of olivines; these absorptions are discussed further below. Regardless of whether the measured olivines are natural or synthetic, their infrared spectra exhibit a generally linear decrease in the wavenumber position of each band as the molar proportion of Fe increases, and this trend is attributed to the increasing radius and mass of the cation linking the SiO_2 tetrahedra. Although Jäger et al. (1998) found that all of the band shifts in units of wavelength $(\Delta\lambda)$ in the four olivines they examined are proportional to λ^2 (to within 20%), the majority of studies have found that the linear trends for each band are not the same, and this is borne out by Fig. 3**a**, which shows variability in the slopes of the best fit lines from band to band. Burns and Huggins (1972) examined the utility of linear regression equations for Bands 1–5, 7, and 9 for predicting mol% forsterite. They found that the ability of the equations to predict compositions from TIR band positions is very good, providing estimates as close to the true compositions, if not closer, than values determined from X-ray data and cell parameter data, with two exceptions. The first exception was that non-linear band location trends were apparent in spectra of

Please cite this article as: Hamilton, V.E., (2010), doi:10.1016/j.chemer.2009.12.005

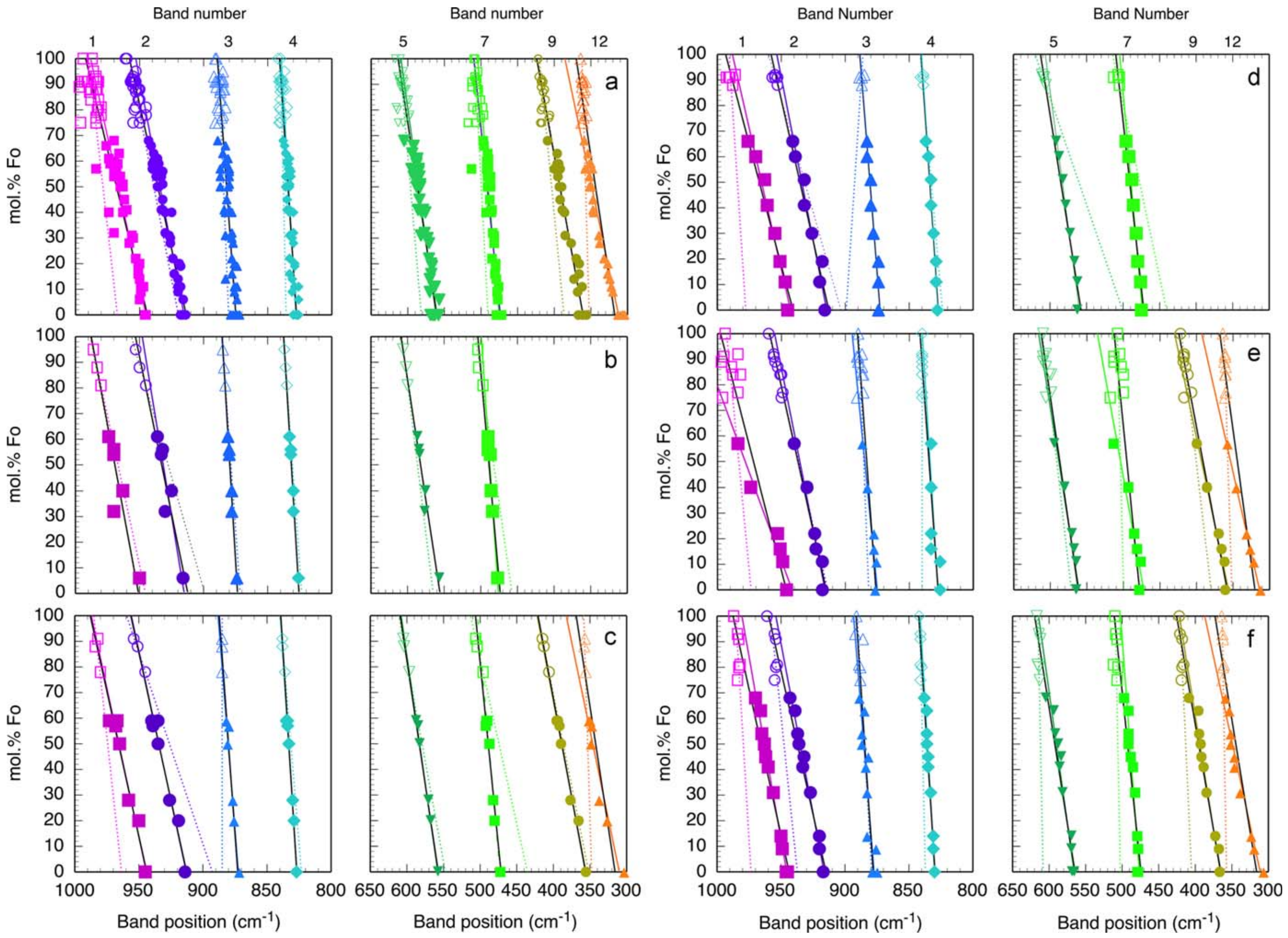

Fig. 3. (a) Infrared band positions in natural and synthetic olivines versus mole percent forsterite from Duke and Stephens (1964) (9 olivines), Burns and Huggins (1972) (10 olivines), Salisbury et al. (1991) (13 olivines), Koike et al. (2003) (16 olivines) and Hofmeister and Pitman (2007) (17 olivines). (b) Infrared band positions from Duke and Stephens (1964); (c) Burns and Huggins (1972); (d) Salisbury et al. (1992); (e) Koike et al. (2003) and (f) Hofmeister and Pitman (2007). Band numbers are as defined by Burns and Huggins (1972). The data of Duke and Stephens (1964) and Salisbury et al. (1991) do not extend beyond 400 cm^{-1}. Black lines denote a linear fit to all data for a given band. Solid colored lines denote linear fit to data representing compositions $<$Fo$_{70}$ (solid symbols) and dotted colored lines denote linear fit to data representing compositions $>$Fo$_{70}$ (open symbols).

compositions in the olivine series that exhibit greater ordering (i.e., Mg–Mn and Fe–Mn). These investigators therefore concluded that the linearity of band positions as a function of composition in the forsterite–fayalite series indicates a nearly random distribution of Mg^{2+} and Fe^{2+} in the M1 and M2 sites and that any significant deviation from linearity would indicate ordering of the Mg^{2+} and Fe^{2+} ions. They found a second exception in the case of two fayalite samples, where the linear equations showed greater maximum deviations than were typical for determination of mol% forsterite. Burns and Huggins (1972) interpreted this greater deviation in the fayalites to indicate the presence of another cation, probably Mn^{2+}, which commonly substitutes for Fe^{2+} (where their analysis of the fayalite–tephroite (Mn$_2$SiO$_4$) solid solution suggests a similar linear function of band positions vs. substituent cation).

Although comprised of data from multiple investigators, measured at varying spectral range and, in some cases, resolution, the combined data shown in Fig. 3**a** exhibit consistent results, and almost all have strong linear correlations (Table 2). The bands with the highest R^2 values (2, 9, 5, 1, and 12) should be the best bands for determination of accurate Mg–Fe composition from TIR transmission spectra, as they are the most repeatable across all studies shown here. The 2-sigma standard errors associated with the fits to these bands indicate that these equations can be used to predict composition to within $\pm$6–10 mol% forsterite. Fig. 3**b–f** provides a detailed view of the linear fits to each band in the individual data sets.

For many years, the idea persisted that olivine band positions shifted linearly across the full range of Mg–Fe compositions; however, Koike et al. (2003) and Hofmeister and Pitman (2007) showed that this is not always the case. Koike et al. (2003) did not provide linear regression fits to their data but their figures reveal that some positions do not follow a perfectly linear trend across the full binary, and that some features display offsets in spectra representing samples having moderate to high Mg contents. The regression analysis of band positions in TIR thin-film spectra by Hofmeister and Pitman (2007) showed that some bands are better described by two linear equations, where the transition from one equation to the other appears to occur near Fo$_{70}$. They also observed that in addition to a different linear slope, there may also be discontinuities, or offsets, between the two equations that are larger than the uncertainties in the band positions. Hofmeister and Pitman (2007) demonstrated these trends using band positions derived from Lorentzian curve fits; using this approach, they were able to map peak positions not readily observed as minima in the TIR spectra. Fig. 3**f** shows the positions of the observable spectral peaks in their data for Bands 1–5, 7, 9, and 12,

Please cite this article as: Hamilton, V.E., (2010), doi:10.1016/j.chemer.2009.12.005

Table 1
Olivine transmittance band positions (cm^{-1}).

$Fo_{\#}$	Band 1	Band 2	Band 3	Band 4	Band 5	Band 6	Band 7	Band 8	Band 9	Band 10	Band 11	Band 12	Band 13
Salisbury et al. (1991b)													
91	991	957	889	841	610	542	507	461	419				
91	986	955	885	839	611	544	507	461	424				
91	993	955	889	841	610	542	513	461	422				
91	988	953	887	839	606	540	505	459	417				
88	990	953	887	839	608	540	505	461	415				
66	976	941	883	837	592	515	496	–	405				
60	970	939	883	835	588	513	492	–					
51	963	932	880	833	583	511	488	–					
41	961	932	880	833	579	515	486	(413)					
29	955	926	878	831	573	513	482	411					
18	951	918	874	829	567	511	480	411					
11	947	920	874	829	563	507	476	409					
1	945	916	874	828	563	505	475	(419)					
Hofmeister and Pitman (2007)													
100	987	961	891	842	617	(528)	510	476	422	405	383	364	296
93	984	955	892	841	614	524	509	471	421	(402)	380	363	294
91	983	954	886	841	612	525	507	470	418	(400)	378	362	294
81	982	953	889	841	616	523	512	468	416	(398)	377	361	294
80	983	954	888	840	614	522	506	468	418	(399)	378	362	294
75	984	955	888	841	613	524	507	471	419	(402)	380	363	294
68	970	943	889	838	605	519	497	(460)	409	–	–	359	288
63	966	939	885	836	594	516	491	–	396	–	–	354	284
54	965	937	887	836	592	516	491	–	395	–	–	352	282
50	963	936	887	836	588	516	491	–	393	–	–	352	(279)
45	962	932	882	835	584	516	488	–	392	–	–	347	–
41	960	933	884	835	586	514	485	–	389	–	–	347	–
31	956	927	883	833	582	516	482	(417)	385	–	–	339	–
14	950	920	883	831	570	506	479	(407)	373	–	–	324	–
9	949	920	876	831	570	506	478	(413)	368	–	–	320	–
0	945	917	875	830	566	507	478	–	367	–	–	307	–
0	946	917	879	830	569	505	479	(418)	367	–	–	307	–

Band positions in parenthesis indicate very weak minima or shoulders; Salisbury et al. (1991b) data do not extend past 400 cm^{-1}.

Table 2
Regression data for linear fits to transmittance band positions.

Band number	Regression equation(Fo_{0-100})	R^2 (Fo_{0-100})	2σ Std. Err. (Fo_{0-100})	R^2(Fo_{0-70})	R^2(Fo_{70-100})
1	$f(x)=1.88 \times x-1772.38$	0.910	9.56	0.837	0.088
2	$f(x)=2.18 \times x-1985.90$	0.963	6.15	0.936	0.499
3	$f(x)=5.31 \times x-4634.59$	0.760	15.61	0.597	0.050
4	$f(x)=6.38 \times x-5273.64$	0.842	12.65	0.686	0.029
5	$f(x)=1.75 \times x-977.00$	0.928	8.52	0.878	0.143
7	$f(x)=2.35 \times x-1102.92$	0.849	12.37	0.721	0.055
9	$f(x)=1.52 \times x-545.48$	0.961	6.48	0.925	0.338
12	$f(x)=1.72 \times x-539.40$	0.903	10.20	0.946	0.126

along with linear trends for: (1) the entire binary range of compositions, (2) compositions $<Fo_{70}$, and (3) compositions $>Fo_{70}$. Although linear fits work reasonably well for the entire range of Mg–Fe compositions, linear fits to the $<Fo_{70}$ and $>Fo_{70}$ points show that Bands 1, 2, 5, 7, 9, and 12 display a clear break in the slope of the best fit lines. For Bands 1, 2, 5, and 9, this break in slope is accompanied by an offset, to higher wavenumbers, of the positions in spectra representing the most Mg-rich compositions. Similar comparisons are shown for the other individual data sets in Fig. 3**b–f**. The data of Duke and Stephens (1964) (Fig. 3**b**) do not display breaks in slope, or any apparent offsets. The band positions recorded by Burns and Huggins (1972) for Bands 1–3, 7, and 9 display differing trends on either side of Fo_{70} (Fig. 3**c**); however, their trends do not always show the generally steeper slope for the fit to $>Fo_{70}$ as observed by Hofmeister and Pitman (2007) (Fig. 3**f**). The fits to band positions for compositions $>Fo_{70}$ in the data of Salisbury et al. (1991b) cannot be reliably fit by a linear equation (Fig. 3**d**), because they are based on a very narrow range of compositions (Fo_{88-92}). Linear fits to the band positions in the data of Koike et al. (2003) demonstrate quantitatively what was qualitatively observable in their paper—several bands appear to be better described by two linear equations and exhibit offsets, although the break in slope in their data seems to occur closer to Fo_{60} for Bands 1, 7, and 12 (Fig. 3**e**). For several bands, there is greater scatter in the positions reported by Koike et al. (2003) than for the other data sets; this may be an artifact of their measurement approach. Hofmeister and Pitman (2007) argue that spectra acquired using pressed powder pellets (the powder dispersion method, used by the other transmission studies described here) are not sufficiently accurate to identify these trends because they are subject to inaccuracies attributable to variations in the optical depth of the sample. These inaccuracies result in the rounding of strong band features and the artificial strengthening of weak peaks and shoulders, which can lead to

Please cite this article as: Hamilton, V.E., (2010), doi:10.1016/j.chemer.2009.12.005

difficulty in identifying band positions and apparent band shifts. Despite these potential inaccuracies, Fig. 3**a** suggests that the combined band position data from 65 olivine samples (48 of which are derived from powder dispersion data) is adequate to distinguish at least the break in linear slope near Fo_{70} in Bands 1, 9, 12, and possibly 5. An offset at Fo_{70} may be inferred from the fits to the Band 1 data, but the scatter in the data for samples $>Fo_{70}$ (R^2=0.09, Table 2) makes this a tenuous inference at best.

Hofmeister and Pitman (2007) attribute the breaks in slope and offsets in the linear trends at Fo_{70} to a structural variation that occurs abruptly near this composition. They infer this because changes in cation mass occur linearly across the solid solution series, so bond strength should also change linearly. They point out, however, that it is likely that bond lengths do not change linearly across the solid solution series, as unit cell volume and one of the lattice parameters are non-linear functions of mol% forsterite. Bond lengths change with distortion of the lattice, so the composition at which the trend changes is related to the relative sizes of the Mg and Fe cations; Mg is smaller than Fe and does not distort the lattice when it is present, but Fe is larger and distorts the region around the octahedral site which it inhabits. As such, modest Fe substitution (~30%) in forsterite is sufficient to distort the structure and change the trend of the observed band positions.

In addition to band shifts with cation substitution, relative band intensities change as well (e.g., Burns and Huggins, 1972; Reynard, 1991; Jäger et al., 1998; Koike et al., 2003). Although Bands 1–7 are present across the solid solution series, Bands 8, 10–13 are apparent only in magnesium-rich compositions greater than ~Fo_{70}. Bands 6, 9, and 12 exhibit discernible variations in strength as a function of composition. Band 6 is only a shoulder in the spectra of Mg-rich compositions, but develops into a discernible peak (or minimum) with increasing iron content (the composition at which this transition occurs varies between the data sets referenced here); Burns and Huggins (1972) attribute this to divergence of Bands 6 and 7. Band 9 is stronger than Band 12 in forsteritic olivines, but this relationship is reversed in fayalitic olivines, and the transition appears to be generally linear across the compositional range (e.g., Fig. 2, the band strengths are essentially equivalent at ~Fo_{45-50}), consistent with these bands having their origins in motions of the cations and the lattice, rather than being related to the bending modes of the silicon tetrahedra.

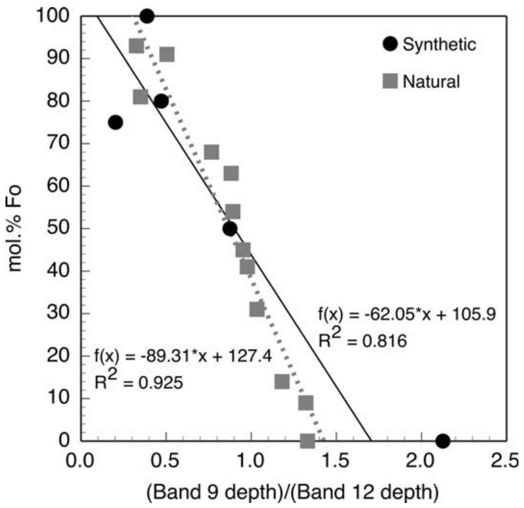

Fig. 4. Ratio of Band 9 absorbance to Band 12 absorbance versus mol% forsterite for spectra acquired by Hofmeister and Pitman (2007). Solid line describes a linear fit to the entire data set (natural and synthetic samples), and dotted line describes a linear fit to ratios obtained from spectra of natural samples.

Fig. 4 shows the relationship between the ratio of the depth of Band 9 to that of Band 12 and composition (mol% forsterite) for the Hofmeister and Pitman (2007) spectra shown in Fig. 2. The linear fit to all data, representing spectra of both natural and synthetic samples, exhibits a good correlation (R^2=0.816) with a 2-sigma standard error of 14.6, indicating that this linear relationship will be accurate in predicting mol% forsterite from this band depth ratio to ~±15 mol% in 95% of cases. Because synthetic samples may not produce spectra that exhibit identical characteristics as natural samples, the linear fit to only the natural samples also is shown. When synthetic samples are excluded, the coefficient of determination is excellent (R^2=0.925), and the 2-sigma standard error is 9.1, indicating that this linear relationship will be accurate in predicting mol% forsterite from this band depth ratio to ~±9mol% in 95% of cases.

2.4. *Reflection data—spectral trends as a function of solid solution composition*

Unpolarized infrared reflectance spectra of randomly oriented olivine particulate samples have not been studied at the same level of detail as that described for transmission data in Section 2.3, but offer a similar perspective on the presence or absence of spectral features and the relationships between olivine composition and band position. The two most complete sets of publicly available reflectance spectra for a range of olivine compositions prepared in a consistent manner have been published by Salisbury et al. (1991b) and Clark et al. (2007). Between these two studies, 14 natural olivines were analyzed, with nine physical samples common to both. The measured samples are particulates, all of which are <165 μm. All of the Salisbury et al. measurements were made with an unmodified biconical reflectance attachment, and thus may exhibit distortion around the Christiansen feature. Therefore, measurements acquired by Clark et al. (2007) are used for the analysis here (acquired with 2 cm^{-1} spectral sampling), and the only spectra from the Salisbury et al. (1991b) library that are included are those that were not re-measured by Clark and coworkers. Any distortions in the Salisbury et al. (1991b) data should only affect the analysis of the Christiansen feature, and are described below. Note that the Salisbury et al. (1991b) data extend only to 400 cm^{-1}, and the Clark et al. (2007) data in some cases include the range out to 200 cm^{-1}.

Fig. 5 shows infrared reflectance spectra of 14 natural olivines (sample chemistries and details of sample preparation and spectral data acquisition may be found in Salisbury et al. (1991b) and Clark et al. (2007)). Table 3 lists the positions of spectral features. As expected, the observed general trend is that of band positions shifting to lower wavenumbers as a function of decreasing mol% forsterite (Fig. 6). The band positions are well fit by linear trends (Table 4); unfortunately, although there are five samples with >70 mol% forsterite, the compositions are too similar to derive a good linear fit and evaluate whether the break in trend observed for transmittance data is also observable in reflectance spectra. As in the transmittance spectra, it seems that Bands 8, 10, 11, and 13 disappear with decreasing mol% forsterite, although from the available data, it is only possible to say that these features are present in the spectrum of a sample having a composition of Fo_{91} and are not visible (or are weak in the case of Band 13) in the spectra of samples with Fo_{19-66}. Bands 9 and 12 are outside the range of available data for three of the most Fe-rich compositions (Fo_1, Fo_{11}, and Fo_{30}), so the trend lines in Fig. 6 do not include these samples. As described above for

Please cite this article as: Hamilton, V.E., (2010), doi:10.1016/j.chemer.2009.12.005

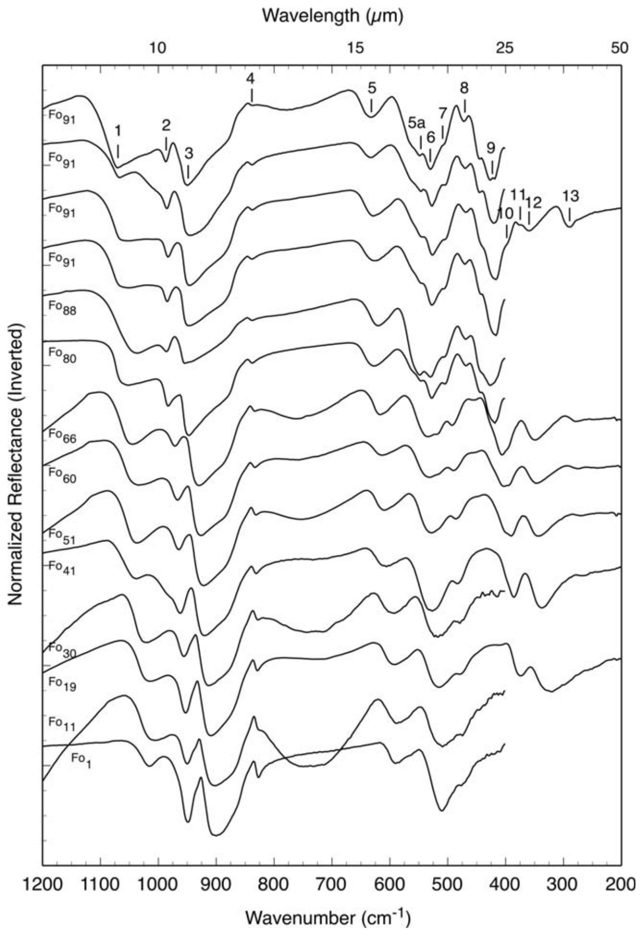

Fig. 5. Reflectance spectra of 14 natural Mg–Fe series olivines from Salisbury et al. (1991) and Clark et al. (2007). Sample numbers/names for spectra representing compositions of Fo_{91} are, from the top down, NMNH-137044, Wards Natural Science Establishment (WNS), GDS70, and GDS71.a. Band numbers are as defined by Burns and Huggins (1972), with the exception of Band 5a, which is not present in transmission data (see text for discussion). Most spectra were acquired of powder samples with mean particle sizes of 65 μm or less, except two Fo_{91} samples (WNS and GDS70), Fo_{80}, and Fo_1, which are coarse particulates with particle sizes ≥ 75 μm. Slopes at high wavenumbers ($>1050\ cm^{-1}$) and minima between the reststrahlen bands (e.g., Fo_{11}, near $725\ cm^{-1}$) are transparency features attributable to volume scattering. Spectra are offset for clarity, and shown as inverse reflectance ($E=1-R$) for comparison with spectral data in other figures.

transmittance spectra, Band 9 increases in strength and Band 12 decreases in strength as the iron content in olivines increases. The band strength ratio for Bands 9 and 12 in the six spectra for which these bands are measured is described well by a linear fit (Fig. 7). As suggested above, this transitional behavior is linear with composition—band depth ratios <1.0 are indicative of Mg-rich olivines, whereas ratios >1.0 indicate Fe-rich compositions. A trend not clearly observed in transmittance spectra is the increasing strength of Band 2 with increasing iron content (Fig. 5). Also, a significant difference between the transmittance and reflectance spectra is the presence of a shoulder/band between Bands 5 and 6 (Fig. 5), referred to here as Band 5a, although this is not intended to denote a relationship to Band 5. Band 5a is a weak shoulder in Mg-rich compositions, but becomes stronger with increasing iron content; it is likely attributable to splitting of the degenerate ν_4 asymmetric bending vibration. Band 5a is a discernible minimum in the spectrum of Fo_{88} olivine, and at $\leq Fo_{66}$ is stronger than Band 6, which disappears in the spectrum of Fo_{60} olivine. Band 7 also becomes stronger with increasing iron content, changing from a shoulder in compositions greater than $\sim Fo_{80}$ to an obvious minimum in spectra of samples $\leq Fo_{66}$.

The Christiansen feature (CF), as described above, is located on the high wavenumber side of the silicate stretching bands in reflectance and emissivity data, where the real part of the refractive index changes rapidly and approaches the refractive index of the surrounding medium (e.g., air). Because scattering is minimized and absorption is low, infrared radiation passes through the sample easily, and a reflectance minimum (emissivity maximum) is observed. The position of this feature in silicate minerals has been shown to shift to lower wavenumbers (longer wavelengths) with decreasing polymerization of the silicate structure (Conel, 1969; Salisbury et al., 1987). Even though the optical constants are invariant, environmental factors (e.g., measurement technique, vacuum, spectral resolution) may cause the position of this feature to shift, so comparisons of like data are required to use this feature as an indicator of composition. In silicate spectra, a second, similar feature is observed on the high wavenumber (short wavelength) side of the absorption features resulting from silicate bending modes. Because the feature adjacent to the silicate stretching bands has been referred to in the literature as the "primary" Christiansen feature (e.g., Salisbury et al., 1991a), the feature at lower wavenumbers has been described as the "secondary" Christiansen feature (Hamilton, 2000). Here I will abbreviate these features as CF1 and CF2, respectively. To determine whether the positions of the CFs within the olivine solid solution series are correlated with composition, I have plotted in Fig. 8a and b the positions of CF1 and CF2 versus mol% forsterite for the 14 samples shown in Fig. 5. There are good linear correlations between composition and the positions of CF1 ($R^2=0.937$) and CF2 ($R^2=0.968$), indicating that the positions of the CFs are diagnostic of Mg:Fe in olivines. The 2-sigma standard errors for these correlations are 8.6 for CF1 and 6.2 for CF2. Although the position of CF1 in reflectance data can be affected by the instrumental configuration, it does not appear to be strongly affected by differences between the measurements of Salisbury et al. (1991a) and Clark et al. (2007) used here.

2.5. *Emission data—spectral trends as a function of solid solution composition*

Here I present a data set comprised of new olivine emissivity spectra as well as near-end member compositions from published sources. The samples and spectra of Fo_{92}, Fo_{90}, and Fo_0 are from the Arizona State University spectral library (Christensen et al., 2000b). The remainder of the spectra are presented here at full laboratory resolution for the first time; the olivines from which they were measured were collected from the Kiglapait Intrusion of north coastal Labrador and provided by S. A. Morse. The Kiglapait olivines and their genetic relationship in the context of this layered mafic intrusion are described in Morse (1996), and their infrared spectra were collected by Koeppen and Hamilton (2008). Sample chemistries are provided in Table 5. All samples consist of coarse (>125 μm) particulates. Thermal emission spectra of the samples from the ASU spectral library were acquired on a ThermoNicolet Nexus 670 FTIR, as described by Ruff et al. (1997) and Christensen et al. (2000b). Emissivity spectra of the Kiglapait olivine samples were measured using a similarly configured ThermoNicolet Nexus 470 FTIR spectrometer (Hamilton and Lucey, 2005). All spectra, unless indicated otherwise, are the average of 270 scans at $2\ cm^{-1}$ sampling ($4\ cm^{-1}$ resolution). These data are available in the Arizona State University online spectral library (Christensen et al., 2000b).

Fig. 9 shows the emissivity spectra of 11 natural olivines (a 3-point boxcar filter has been applied twice to minimize noise),

Please cite this article as: Hamilton, V.E., (2010), doi:10.1016/j.chemer.2009.12.005

Table 3
Olivine reflectance band positions in wavenumbers (cm^{-1}).

Sample	CF1	CF2	Fo#	Band 1	Band 2	Band 3	Band 4	Band 5	Band 5a	Band 6	Band 7	Band 8	Band 9	Band 10	Band 11	Band 12	Band 13
NMNH-137044[b]	1138	673	91	1071	988	951	839	635	548	530	507	473	426				
WNS[b]	1131	669	91	1067	986	947	839	633	546	527	503	469	421				
GDS70[a]	1123	669	91	1051	984	945	837	629	542	527	505	469	417	(397)	(374)	359	289
GDS71.a[a]	1127	669	91	1051	984	947	837	625	544	527	505	471	417				
Brenham[b]	1130	664	88	1038	986	955	839	621	548	530	507	469	426				
HS-285.4b[a]	1128	669	80	1051	984	947	837	627	546	527	505	469	419				
KI3054[a]	1103	650	66	1044	970	928	833	617	534	521	492	457	407	–	–	349	278
KI3189[a]	1096	646	60	1034	966	926	833	613	530	(513)	490	–	403	–	–	347	274
KI3188[a]	1088	640	51	1038	964	922	831	610	529	–	486	–	390	–	–	343	270
KI4143[a]	1088	642	41	1038	963	920	831	606	527	–	484	–	386	–	–	338	264
KI3291[a]	1063	629	30	1018	957	914	828	594	517	–	478	–					
KI3377[a]	1065	629	19	1015	953	909	829	592	515	–	480	(409)	374			320	
KI3005[a]	1057	621	11	1005	951	903	824	588	509	–	475	–					
NMNH-R3517[b]	1065	617	0	1015	949	901	828	590	509	–	476	–					
GSB (GDS70)[b]	1123	667	91	1073	988	951	839	635	550	529	507	469	424				
TSD (GDS71)[b]	1134	671	91	1051	988	953	839	627	550	530	507	471	428				
KI3054[b]	1115	656	66	1053	976	937	833	619	544	(523)	496	453	411				
KI3189[b]	1111	650	60	1038	972	932	833	615	540	(519)	492	448	407				
KI3188[b]	1098	646	51	1036	968	930	831	611	536	–	488	–					
KI4143[b]	1090	642	41	1038	963	920	829	606	529	–	484	–					
KI3291[b]	1078	635	30	1026	961	920	829	598	527	–	486	–					
KI3377[b]	1071	631	19	1020	955	912	829	594	519	–	482	–					
KI3005[b]	1064	623	11	1007	955	912	828	577	517	–	478	–					

Blank cells indicate band is outside range of data or no data were available ($< 400\ cm^{-1}$), parentheses indicate weak band or shoulder, "–" indicates no feature is visible.

[a] Positions measured from spectra acquired by Clark et al. (2007).

[b] Positions measured from spectra acquired by Salisbury et al. (1992)—data below the dotted line are not included in figures.

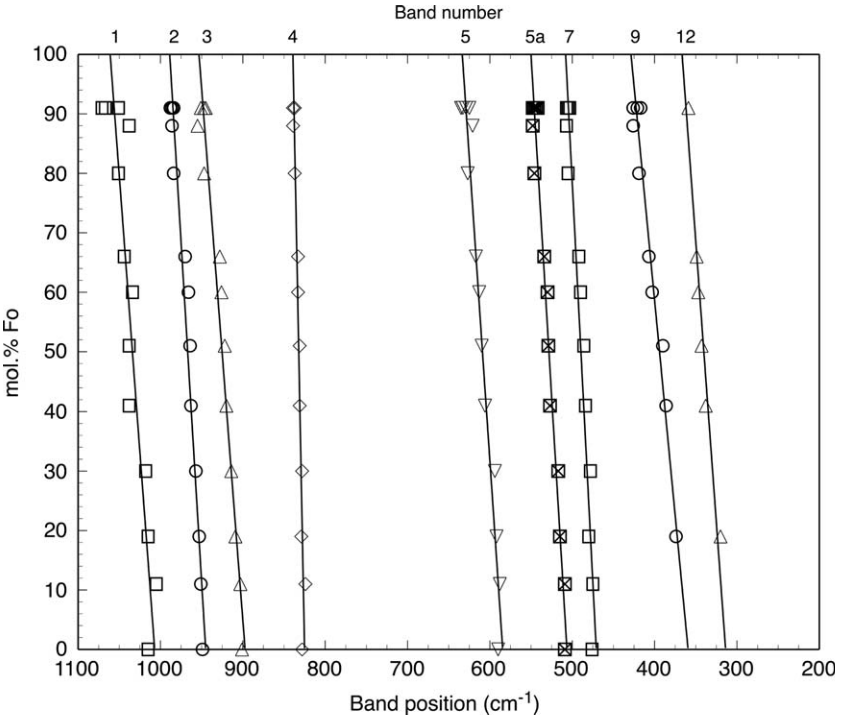

Fig. 6. Reflectance band positions in 14 natural olivines (shown in Fig. 4) versus mol% forsterite. Data are from Clark et al. (2007). Band numbers are as defined by Burns and Huggins (1972), except for Band 5a which is not present in transmission data (see text for explanation). Linear fits to the measured data are shown.

which display the expected trends of absorption bands shifting to lower wavenumber with decreasing mol% forsterite (Fig. 10 and Table 6). All nine of the measured band shifts can be fit with linear equations having coefficients of determination (R^2) that indicate 92–99% of the data can be accounted for by the linear regression equations (Table 7). As with the reflectance data, there is not sufficient data for a range of compositions $> Fo_{70}$ (in particular the lack of a composition between Fo_{68} and Fo_{90}) to determine if the kinks observed in the band position trends of transmittance data are observable in emissivity data; however, if the origin of the kinks lies in structural changes associated with Mg:Fe, the kinks are expected (assuming the measurement technique and/or spectral resolution are adequate to resolve them). If they are present, the linear regressions shown here may introduce additional small uncertainty into the determination of mol% forsterite in compositions between about Fo_{70} and Fo_{90}.

Table 4
Regression data for linear fits to reflectance band positions.

Band number	Regression equation (Fo_{0-100})	R^2 (Fo_{0-100})	2σ Std. Err. (Fo_{0-100})
1	$f(x)=1.50 \times x-1503.75$	0.812	14.82
2	$f(x)=2.20 \times x-2077.85$	0.961	6.72
3	$f(x)=1.70 \times x-1526.78$	0.955	7.29
4	$f(x)=6.40 \times x-5272.41$	0.906	10.50
5	$f(x)=1.93 \times x-1123.66$	0.947	7.86
5a	$f(x)=2.22 \times x-1120.69$	0.967	6.19
7	$f(x)=2.52 \times x-1185.12$	0.939	8.47
9	$f(x)=1.37 \times x-488.54$	0.949	5.90
12	$f(x)=1.81 \times x-565.69$	0.957	5.62

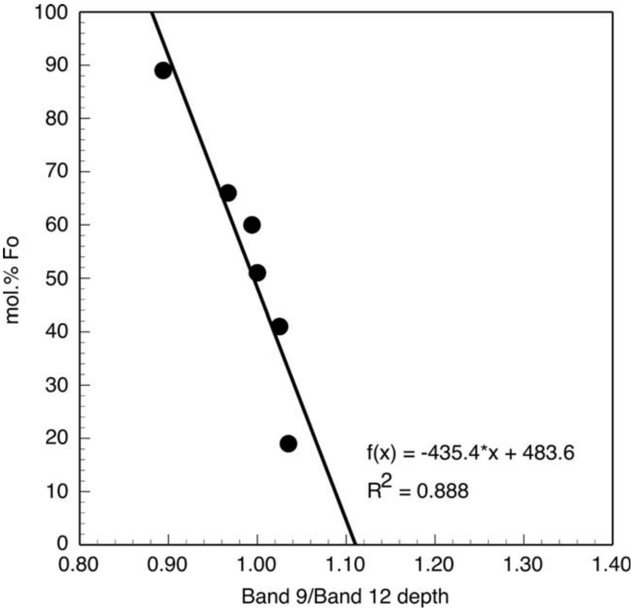

Fig. 7. Ratio of Band 9 reflectance to Band 12 reflectance versus mol% forsterite for spectra acquired by Clark et al. (2007). Equation describes a linear fit to the data (solid line).

As with the transmittance and reflectance spectra described above, Bands 1–4 are present across the Mg–Fe compositional range. The positions of their minima span a wider range of wavenumbers in emission (and reflection) data than in transmission data, and transmission data show much greater overlap in the positions of Bands 1–3, whereas these features do not occur at overlapping frequencies in emission data (Fig. 11). Band 2 strengthens with increasing iron content as observed in the reflectance spectra (Fig. 9). Also as seen in the reflectance spectra, there is a band between Bands 5 and 6 that is referred to here as Band 5a and is probably related to the ν_4 asymmetric bending vibration. Band 5a is a shoulder on the high wavenumber side of Band 6 in forsteritic samples; this shoulder becomes stronger and deepens into a minimum as Band 6 diminishes and disappears with increasing iron content. Bands 8, 10, 11, and 13 diminish in strength with decreasing mol% forsterite. Band 8 is not visible in spectra of compositions more iron-rich than Fo_{54}, Band 10 is only visible as a shoulder in spectra of Fo_{90-92}, Band 11 is only present as a very weak dip in Fo_{92}, and Band 13 (or the peak defining the high wavenumber side of Band 13) is not distinguishable in the spectra of compositions $\leq Fo_{54}$ (Fig. 9). The locations and ranges of position for Bands 5, 7, 9, and 12 are similar to their transmittance counterparts and exhibit minimal overlap (Fig. 11). (A small feature present on the low wavenumber side of Band 12 in some spectra may be attributable to water vapor.) Consistent with the observations from reflectance spectra above, Band 9 shallows and Band 12 deepens with increasing fayalite content—the trend for these bands is linear across the compositional range (Fig. 12). For olivines ranging in composition from Fo_{92} to Fo_0, the ratio of the emissivity in Band 9 to that in Band 12 is described well (R^2=0.915) by a linear function that predicts the Bands 9 and 12 depths should be equivalent at approximately Fo_{54}, with ratios <1.0 indicating a forsteritic composition and ratios >1.0 indicating a fayalitic composition. The 2-sigma standard error indicates that mol% forsterite will be accurately determined to within ± 9.5 in 95% of cases. It is interesting to note that the ratio values for Fo_{92} and Fo_0 fall the farthest from this trend line; if these points are excluded from the linear regression, the best fit trend line fits the remaining data points remarkably well (R^2=0.993), and mol% forsterite will be predicted very accurately from the band ratio (2-sigma standard error of 2.4, or ± 2.4 mol% forsterite). Despite the excellent linear fit to the entire data set, it may be useful to consider why the Fo_{92} and Fo_0 samples plot further from the trend line or, conversely, why the other samples exhibit such a high coefficient of determination in the absence of these two samples. One possible explanation lies in the degree of variability

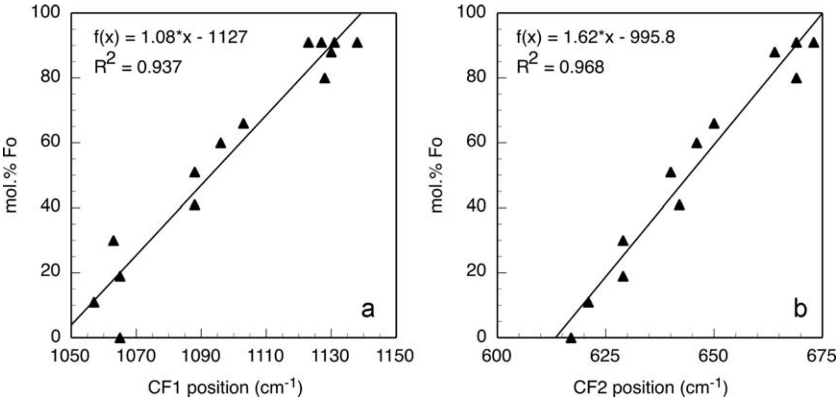

Fig. 8. (a) Position of CF1 versus mol% forsterite in olivine reflectance spectra and (b) position of CF2 versus mol% forsterite. Equations describe linear fits to the data (solid lines).

Please cite this article as: Hamilton, V.E., (2010), doi:10.1016/j.chemer.2009.12.005

Table 5
Olivine sample chemistries.

	BUR-3720A[a]	AZ-01[a]	KI 3115[b]	KI 3362[b]	KI 3372[c]	KI 4143[b]	KI 3373[b]	KI 3352[b]	KI 3354[b]	KI 3008[b]	WAR-FAY01[c]
SiO_2	41.95	38.47	37.40	34.91	35.17	33.36	32.83	31.33	31.06	30.11	29.27
TiO_2	0.01	0.01	0.01	0.01	0.00	0.05	0.02	0.01	0.02	0.03	–
FeO	8.49	9.57	29.01	34.04	38.77	48.71	50.75	56.46	60.43	64.00	67.51
MnO	0.13	0.13	0.40	0.41	0.52	0.76	0.86	1.00	1.13	1.55	2.13
MgO	49.33	48.88	33.93	29.17	25.59	17.36	15.23	10.56	7.50	3.84	0.07
CaO	0.38	0.14	0.05	0.03	0.03	0.18	0.08	0.11	0.14	0.01	0.10
Total	100.29	97.20	100.80	98.57	100.08	100.42	99.77	99.47	100.28	99.54	99.08
Fo	0.91	0.90	0.67	0.60	0.54	0.38	0.34	0.25	0.18	0.10	0.00
Fa	0.09	0.10	0.32	0.39	0.46	0.60	0.64	0.74	0.80	0.88	0.97
Mn	0.00	0.00	0.00	0.01	0.01	0.01	0.01	0.01	0.02	0.02	0.03
Ca	0.01	0.00	0.00	0.00	0.00	0.00	0.01	0.00	0.00	0.00	0.00
X_{Mg}	0.92	0.90	0.68	0.60	0.54	0.39	0.35	0.25	0.18	0.10	0.00

Note: BUR-3720A also contains 0.57 wt% Cr_2O_3; BUR-3720A and AZ-01 chemistries derived from bulk analysis, remainder determined by microprobe analysis.

[a] Christensen et al. (2000b).

[b] Morse (1996).

[c] Koeppen and Hamilton (2008).

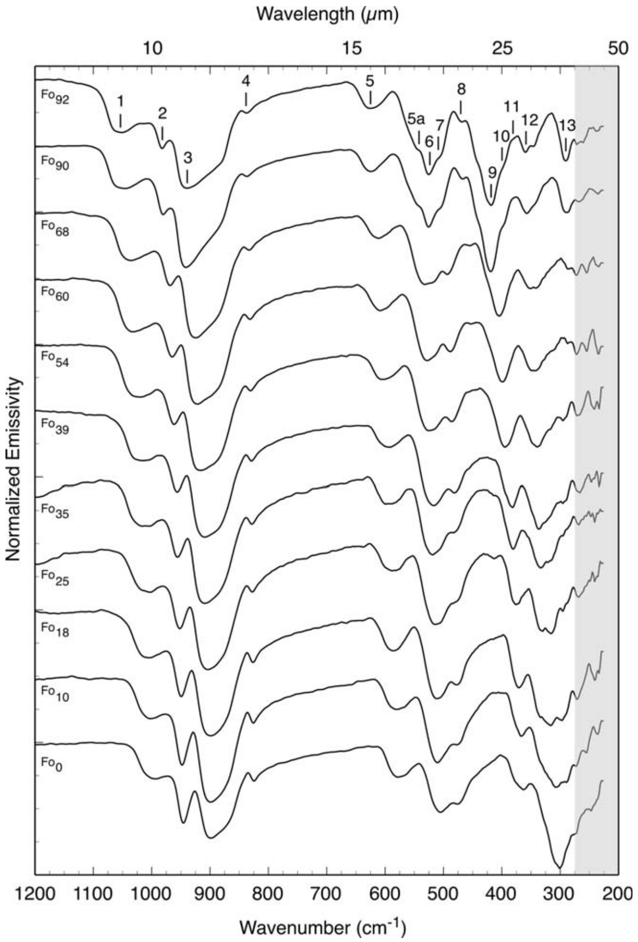

Fig. 9. Emissivity spectra of 11 natural Mg–Fe series olivines (Koeppen and Hamilton, 2008; Christensen et al., 2000). Band numbers are as defined by Burns and Huggins (1972), with the exception of Band 5a (see text for details). Spectra were acquired of coarse particulate (> 125 μm) samples and are normalized and offset for clarity. Gray shaded area indicates region containing additional features attributable to atmospheric water vapor.

in compositional impurities and possible associated cation ordering.

Eight of the 11 olivine samples measured in emission are from the Kiglapait intrusion and are genetically related; the Fo_{92} and Fo_0 samples are not members of this group (Fo_{90} is not a Kiglapait sample, but falls very close to the best fit line and is included in the fit with $R^2=0.993$). The Kiglapait layered mafic intrusion offers a lithologic record of the progressive fractionation of a single mafic magma body. It is plausible, if not likely, that based on their genetic relationship the chemistries of the Kiglapait olivines exhibit a narrower range of variability in the presence and abundance of non-formula elements (i.e., other than Mg, Fe, and Si) than might be expected from a broader suite of natural samples from unrelated parent lithologies. The chemistries reported by Morse (1996) are limited to the oxides shown in Table 5, so a more comprehensive verification of this chemical similarity is not possible, but the available analyses suggest that any additional contaminants must comprise less than about 1.5 wt% oxide (excluding analytical uncertainty). However, broad chemical similarity might result in the spectral properties of these samples being even more tightly tied to Mg–Fe ratio than in a population of non-genetically related samples. This, in turn, could lead to a linear fit to the Band 9/Band 12 ratios for the entire emissivity data set that is weighted by these genetically related samples' spectral character. The natural olivine samples analyzed by Hofmeister and Pitman (2007) offer a point of comparison, as they represent a broad range of compositions across the Mg–Fe binary having differing geologic sources. The Band 9/Band 12 ratios calculated from their transmission spectra (Fig. 4) exhibit a linear trend that is not as well correlated as that derived from emissivity spectra of the Kiglapait samples plus the Fo_{90} olivine ($R^2=0.925$ and 0.993, respectively), but which has a slightly better correlation than the entire emissivity data set ($R^2=0.915$). Five of the six olivine samples with reflectance spectra spanning a broad enough wavenumber range to measure Band 9/Band 12 depth ratios (Fig. 7) also are from the Kiglapait intrusion and offer another point of comparison. The Kiglapait-only samples measured in reflectance exhibit a linear trend with $R^2=0.862$, whereas all six samples yield a modestly better $R^2=0.879$; neither of these is as good as the correlation for the non-genetically related olivines measured in transmission. These comparisons suggest that the genetic relationship between Kiglapait olivines does not lead to a substantially better-correlated spectral trend (at the spectral resolutions considered here) than a suite of randomly sourced olivines.

If a genetic relationship between most of the olivines measured in emission does not explain why the Band 9/Band 12 ratios for Fo_{92} and Fo_0 fall off the best fit line, perhaps contamination of those two samples offers a solution. The Fo_{92} olivine sample contains 0.57 wt% Cr_2O_3 (Christensen et al., 2000b). Because the atomic weight and ionic radius of chromium

Please cite this article as: Hamilton, V.E., (2010), doi:10.1016/j.chemer.2009.12.005

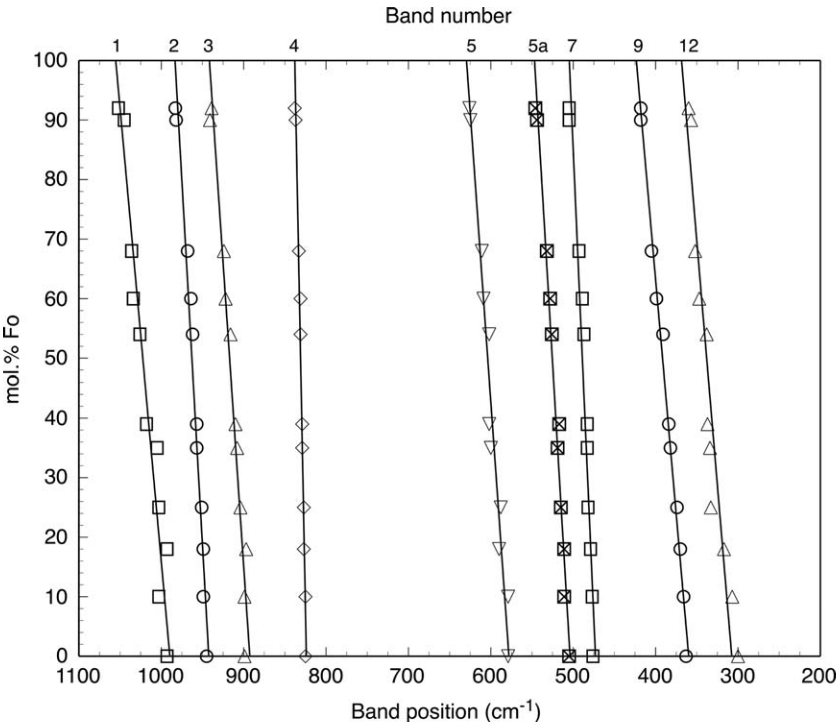

Fig. 10. Positions of emissivity minima in 11 natural olivines versus mol% forsterite. Band numbers are as defined by Burns and Huggins (1972), except for Band 5a. Lines are linear fits to the measured data.

Table 6
Olivine emissivity band positions in wavenumbers (cm^{-1}).

Sample	CF1	CF2	$Fo_{\#}$	Band 1	Band 2	Band 3	Band 4	Band 5	Band 5a	Band 6	Band 7	Band 8	Band 9	Band 10	Band 11	Band 12	Band 13
BUR-3720A	1159[b]	667	92[a]	1052	983	939	838	626	546	525	505	469	418	(393)	(380)	360	291
AZ-01	1117	661	90	1045	982	941	837	625	544	525	505	467	418	(393)	–	357	289
KI 3115	1109	650	68	1036	968	924	833	611	532	(517)	493	455	405	–	–	352	
KI 3362	1111	650	60	1034	964	922	831	609	528	(511)	489	(453)	399	–	–	347	
KI 3372	1101	644	54[a]	1026	962	916	831	602	526	–	487	–	391	–	–	338	
KI 4143	1086	629	39	1018	957	910	829	602	517	–	483	–	384	–	–	337	
KI 3373	1088	629	35	1005	957	908	829	600	519	–	483	(415)	382	–	–	334	
KI 3352	1086	627	25	1003	951	904	827	588	515	–	482	(413)	374	–	–	333	
KI 3354	1082	631	18	993	949	897	827	590	511	–	479	–	370	–	–	317	
KI 3008	1086	619	10	1003	949	899	825	579	511	–	477	–	366	–	–	307	
WARRGFAY01	1072	615	0[a]	993	945	899	825	579	505	–	476	–	363	–	–	300	

[a] $Fo_{\#}$s have been recalculated (see text) and vary slightly from Koeppen and Hamilton (2008).

[b] CF1 distorted in this spectrum; not plotted in Fig. 15.

Table 7
Regression data for linear fits to emissivity band positions.

Band number	Regression equation (Fo_{0-100})	R^2 (Fo_{0-100})	2σ Std. Err. (Fo_{0-100})
1	$f(x)=1.43\times x-1415.70$	0.942	7.83
2	$f(x)=2.37\times x-2228.60$	0.971	5.58
3	$f(x)=1.95\times x-1742.80$	0.963	6.30
4	$f(x)=6.93\times x-5711.20$	0.973	5.37
5	$f(x)=1.88\times x-1084.95$	0.970	5.68
5a	$f(x)=2.28\times x-1145.57$	0.981	4.49
7	$f(x)=2.97\times x-1401.51$	0.948	7.41
9	$f(x)=1.56\times x-561.54$	0.994	2.49
12	$f(x)=1.50\times x-456.24$	0.911	9.72

(~52.00 and 0.52 Å) are less than those of iron (55.85 and 0.645 Å) and magnesium (24.31 and 0.78 Å), we might expect the band strengths to bear a greater resemblance to a sample having less Mg and more Fe (a smaller, heavier cation). In such a case, we would expect the band depth ratio to be larger than predicted, which is what is observed. (I do not have data on the valence state of Cr or Fe in these samples, so I have not considered the effects of valence state and any possible paired substitutions.) The Fo_0 sample contains 2.13 wt% MnO, where Mn commonly substitutes for Fe. As with chromium, the atomic weight and ionic radius of manganese (54.94 and 0.46 Å) are less than those of iron (and magnesium), and may result in an exaggeration of the trend observed with increasing iron, leading to a greater divergence between the depths of Bands 9 and 12. Although they did not discuss relative band strengths, Burns and Huggins (1972) did observe that the positions of absorption bands in the forsterite–tephroite and fayalite–tephroite series continue the trends observed in the forsterite–fayalite series, with features moving to increasingly lower wavenumbers as manganese content increases. It seems plausible, then, that the relative strengths of Bands 9 and 12 may continue to diverge with increasing Fe+Mn content, essentially exceeding the trend observed for intermediate olivines that have lower Mn contents. If this is true, many end

Please cite this article as: Hamilton, V.E., (2010), doi:10.1016/j.chemer.2009.12.005

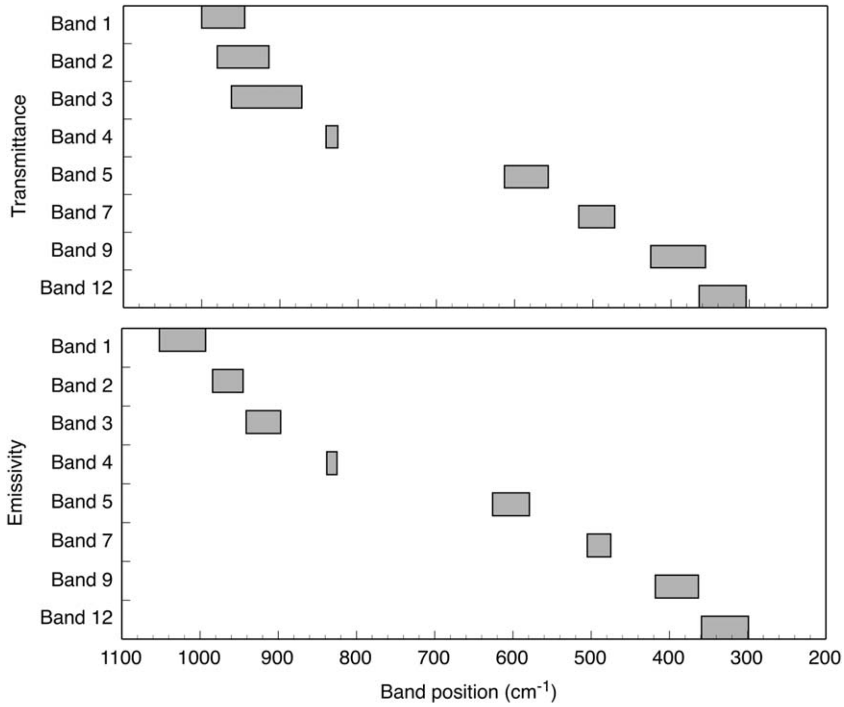

Fig. 11. Range of positions observed in Mg–Fe olivines for absorption bands described in the text.

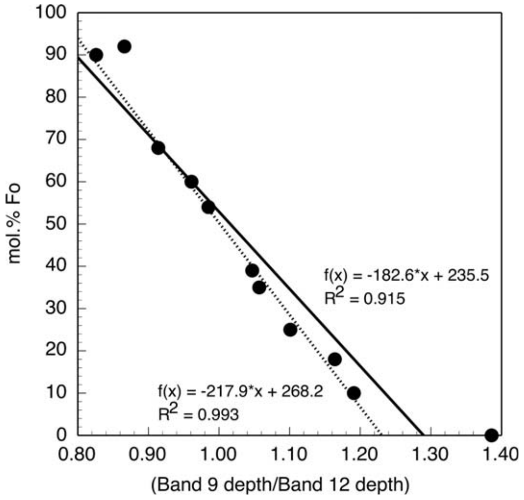

Fig. 12. Ratio of Band 9 emissivity to Band 12 emissivity versus mol% forsterite. Solid line describes a linear fit to all measured data; dotted line describes a linear fit to all measured data except Fo_{92} and Fo_0 (see text for discussion).

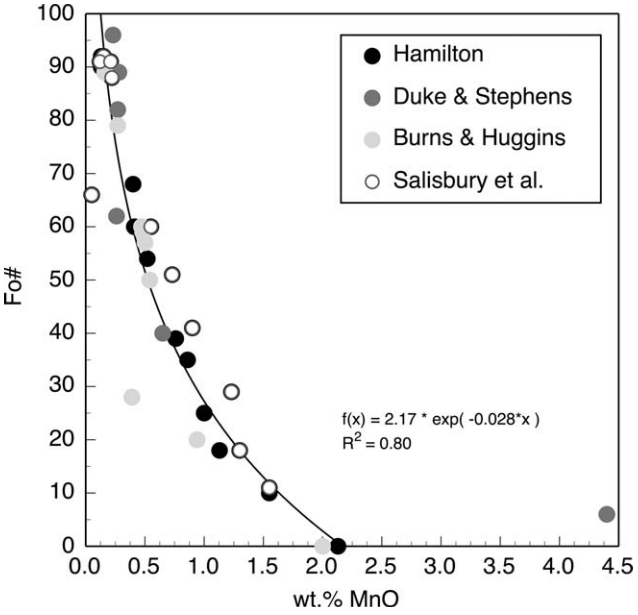

Fig. 13. Weight percent MnO in olivines versus mol% forsterite (as $Fo_{\#}$). Data set includes samples for which detectable MnO was measured by Burns and Huggins (1972)] (10 olivines), Duke and Stephens (1964) (6 olivines), Salisbury et al. (1991) (11 olivines), and in this work (11 olivines). The Fo_{32} sample from Duke and Stephens (1964) is described as exhibiting anomalously high wt% MnO (4.54 wt%) and is not included (the outlier data point with 4.4 wt% MnO also is from Duke and Stephens (1964) but is not explicitly discussed as being anomalous so is included).

member fayalite samples may have spectral features whose ratios diverge from the compositional trend observed here, which is weighted by compositions that naturally contain less Mn. It is worth noting that the band strength ratio observed for this Fo_0 sample is significantly off either of the linear trends shown in Fig. 12. Burns and Huggins (1972) observed that band positions in Mn-olivines do not necessarily shift linearly, which they attribute to the preference of Mn for occupying the M1 site, leading to a non-random distribution of cations (i.e., greater ordering). It is therefore possible that contamination of nearly pure (in terms of Mg:Fe) fayalite by Mn leads to a similarly non-linear divergence in the strengths of Bands 9 and 12. The substitution of Mn for Fe in natural Mg–Fe olivines is quite common, exhibiting a generally exponential increase as olivine becomes increasingly fayalitic (Fig. 13). The commonness of this substitution suggests that spectral trends in band position or depth exhibited by most natural olivines should include the effects of Mn substitution and may become increasingly non-linear at very low $Fo_{\#}$. The spectrum of Mn-bearing fayalite (2.0 wt% MnO, sample #11) shown by Burns and Huggins (1972) exhibits Bands 9 and 12 depths that differ greatly, possibly providing qualitative support for this idea. The quantitative effect of Fe–Mn substitution on band

Please cite this article as: Hamilton, V.E., (2010), doi:10.1016/j.chemer.2009.12.005

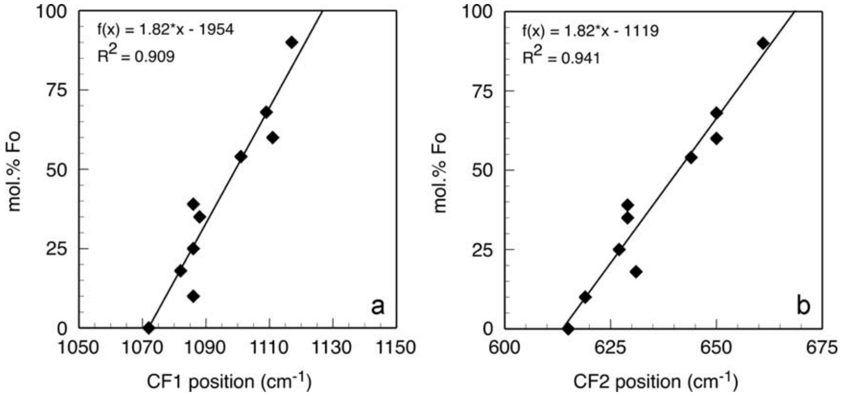

Fig. 14. Positions of CF1 (a) and CF2 (b) versus mol% forsterite in olivine emissivity spectra. Data for sample BUR-3720A are not shown because the spectrum around the primary Christiansen feature is slightly distorted, and therefore unreliable. Equations describe linear fits to the measured data (solid lines).

positions and strengths in the reflectance/emissivity spectra of olivines in the Mg–Fe series may be best studied by a direct comparison of spectra acquired of a series of natural Mg–Fe olivines to a series of synthetic Mg–Fe spectra lacking common substituents such as Mn. Until such analysis is available, we can examine the characteristics of the spectra of fayalites examined in studies to date.

Hofmeister and Pitman (2007) presented transmittance spectra of two fayalite samples, one natural and one synthetic. Fig. 4 shows that the natural fayalite sample's Band 9/Band 12 ratio falls along the best fit line characterizing natural samples measured in transmission. The ratio value for the synthetic sample is substantially higher, and falls well off either the best fit to only natural or both natural and synthetic samples. Detailed compositional data for the natural sample were not provided or readily available, so its Mn content is not known. Compositional data for the synthetic sample indicate that although it does not contain Mn, it could contain from 0.27 to 0.86 wt% Fe^{3+}. The proportion of Fe^{3+} to Fe^{2+} has not been determined for any of the suites of olivines discussed in this paper, so its effect (or that of other cations whose abundance has not been measured) on spectral character cannot be evaluated observationally. However, Fe^{3+} has a smaller ionic radius (0.64 Å) than Fe^{2+} (0.74 Å), suggesting in a simplistic view that its presence might be expected to lead to a greater band depth ratio, as in the cases of Cr and Mn. Although further detailed chemical analysis of a larger number of fayalite samples is required to understand the origins of Band 9/Band 12 ratio values in fayalitic olivines, it is safe to say that high values of the ratio relative to the maximum observed in the linear equations described here indicate a fayalitic composition.

The positions of CF1 and CF2 in emissivity spectra also exhibit linear trends as a function of composition, as observed in reflectance spectra. Fig. 14 shows the correlations between CF1 and mol% forsterite and between CF2 and mol% forsterite. In both cases, the R^2 values associated with the linear fits are >0.90, indicating that better than 90% of the data are explained by the linear equation. For CF1, the 2-sigma standard error is 8.98 and for CF2 the 2-sigma standard error is 7.25. These values indicate that in 95% of cases, the position of CF1 or CF2 can be used to predict olivine solid solution composition to within about ± 9 or 7 mol% forsterite, respectively. The linearity of the shift in CF1 position is consistent with the generally linear shift in the position of Band 1, and the same is true for CF2 and Band 5.

In summary, the shifts in band positions as a function of Mg–Fe observed in emissivity spectra of olivines are linear, similar to those observed for transmittance and reflectance spectra. The linear correlation between the Band 9 and Band 12 depth ratio and mol% forsterite for emissivity spectra is excellent, indicating that this band depth ratio may be used as a diagnostic tool for determining mol% forsterite from emissivity spectra, consistent with the results for reflectance spectra. However, contamination of (near-) end member olivine compositions with non-formula cations may result in greater uncertainties. Regardless of contamination, forsteritic olivines typically have Band 9/Band 12 ratios <1.0 and fayalitic olivines have ratios >1.0. The positions of the primary and secondary Christiansen features also exhibit linear trends, similar to those observed in reflectance spectra, and consistent with the shift in absorption band positions to lower wavenumbers with increasing iron content.

2.6. *Effects of physical character and temperature on olivine spectra*

Crystal orientation and particle shape have an effect on the observed thermal infrared spectra of crystalline silicates, including olivines. Spectra obtained of single crystal olivines and/or acquired using polarized light isolate the vibrational modes along the optic axes of the mineral. Such spectra are commonly acquired for the purpose of ascertaining the true number, position, and assignment of vibrational modes, and/or determining the complex indices of refraction (Servoin and Piriou, 1973; Iishi, 1978; Hofmeister, 1987, 1997; Reynard, 1991; Fabian et al., 2001; Suto et al., 2002). Accurate knowledge of the vibrational modes is required for thermodynamical models, whereas the optical constants may be used for predictive modeling of the spectra of specific particle sizes or shapes. To enable better analysis of circumstellar dust spectra, Fabian et al. (2001) undertook a study to compare the calculated mass absorption coefficients for randomly oriented ellipsoidal particles, spheres, and distributions of ellipsoids to measured powder spectra of olivine. They observed that calculated spectra of olivine spheres least resemble powdered natural olivine, where the natural olivine is best matched by a continuous distribution of ellipsoids, likely due to the irregular particle sizes obtained during mechanical grinding of natural olivine. Peak positions of ellipsoidal olivine shift to longer wavelengths with increasing elongation, although this character is most pronounced in the strongest absorption bands and minor to negligible in the weakest bands. These investigators also determined that the narrower the observed spectral features, the narrower the shape distribution. Although highly relevant to astronomical observations of dust clouds, these spectral characteristics are less relevant to observations of the relatively dense materials on planetary surfaces.

The spectral properties of silicates are known to change with significant variations (differences of up to 293.5 K) in temperature (e.g., Day, 1976; Henning and Mutschke, 1997). Most studies of the temperature-dependent spectral character of olivines in the infrared have been conducted using far infrared to millimeter ($<667\ \mathrm{cm}^{-1}$ or $>15\ \mu\mathrm{m}$) transmission spectroscopy of small particles for comparison to astronomical observations of cosmic dust. These studies have shown that crystalline olivines exhibit stronger, narrower (~30–90% of original width, depending on wavenumber position) features that are shifted 1–5 cm^{-1} to higher frequencies (shorter wavelengths) as temperature decreases from room temperature (295 K) to as low as 1.5–25 K. Band splitting in the ~21–38 μm region of two forsteritic olivine spectra was observed at low temperatures (3.5 K) by Bowey et al. (2001), and are attributed to different polarizations occurring at the same frequency (which are unresolvable at room temperature). The magnitudes of the band shifts and the band narrowing increase with band wavelength (e.g., Mennella et al., 1998; Bowey et al., 2001; Chihara et al., 2001). The increase in frequency is observed because at very low temperatures, the crystal structure contracts, resulting in a reduction in the amplitude of the lattice vibration, which in turn leads to a stronger force constant. The potential well of the lattice vibration becomes deeper and requires additional energy to excite the normal vibrational mode (phonon), shifting the peaks to higher frequencies. The amount of the observed shift is lowest in the features arising from the relatively incompressible tetrahedral Si–O bonds, and is greatest for bands attributable to the more compressible metal cation–oxygen and inter-tetrahedral oxygen atoms (Bowey et al., 2001). The increase in intensity and narrowing of band widths is explained by the reduction in the number of active phonons at low temperature, which leads to a reduced damping coefficient. The small wavenumber values of the observed shifts for large ΔT demonstrate that high spectral resolution (~0.1–0.5 cm^{-1}) is required to fully discern and/or characterize temperature effects in thermal- and far infrared spectra. As in the case of transmission studies of oriented crystals and particle shapes, the direct applicability of these temperature studies to the interpretation of infrared spectra of planetary surfaces observed in the thermal infrared is somewhat limited—these effects are most pronounced in the far IR and require high spectral resolution and signal-to-noise to be observed. The thermal IR spectra of relatively denser and larger particulate materials on planetary surfaces are more likely to be dominated by effects attributable to temperature gradients than by absolute temperature.

The mean particle size and porosity of a bulk material (such as a planetary surface or particulate mineral samples) can affect observed TIR spectral features measured by reflection or emission spectroscopy because these spectra are a result of both the absorption coefficient and the refractive index (whereas transmission spectra are affected only by the absorption coefficient). Numerous investigators have modeled these effects and shown that the measured radiance of particulate materials is affected by two interactions: surface scattering and volume scattering (Vincent and Hunt, 1968; Conel, 1969; Logan and Hunt, 1970; Hunt and Logan, 1972; Hapke, 1981, 1993; Salisbury and Eastes, 1985; Moersch and Christensen, 1991; Salisbury and Wald, 1992; Mustard and Hays, 1997). Whether the measured radiant energy is dominated by surface or volume scattering depends on the absorption coefficient and the particle size, with volume scattering becoming more prominent as the dominant particle size approaches the wavelength of observation (in practice, particle sizes of less than ~65 μm in the thermal infrared). Surface scattering refers to light that is reflected from the surfaces of the particles without penetration. Reflectance and emissivity spectra that are dominated by surface scattering, such as those of coarse particulates and solids, exhibit strong bands (reststrahlen features) in regions with high absorption coefficients and refractive indices and little or no absorption elsewhere. Volume scattering in the thermal infrared arises most commonly in fine particulate (~ < 65 μm) materials as light is refracted into particle interiors and then is scattered or refracted back out. Qualitatively, spectra dominated by volume scattering exhibit reduced contrast in the reststrahlen bands and increased spectral contrast in the interband regions (also called transparency features) where the absorption coefficient is very low, the refractive index is moderate, and photons interact with a large number of interfaces and cannot easily escape. (More detailed qualitative and quantitative descriptions of the wavelength dependency of volume scattering on particle size and the optical constants can be obtained from the citations above.) Understanding these effects is important to distinguishing features due to scattering effects from those due to composition in spectra from planetary surfaces where regoliths may contain dusty or very fine materials (e.g., Christensen and Moore, 1992; Pieters et al., 1993). Reflectance data of olivines collected by Salisbury et al. (1991b) and emissivity data collected by Maturilli et al. (2008) illustrate the decrease in spectral contrast and appearance of additional features that accompanies a decrease in particle size from solid samples down to fine (<65 μm) particulates. Mustard and Hays (1997) examined the effects of particle size in greater detail using reflectance (to 25 μm) spectra of a forsteritic (Fo_{94}) olivine separated into five, 5-μm interval, size fractions from <5 to 20–25 μm. With decreasing particle size, they observed a continuous decrease in the contrast of the reststrahlen bands and some changes in band shape, although the features diagnostic of composition were only mildly affected. Transparency features exhibited several notable changes as particle size decreased: the position of maximum reflectance shifted to shorter wavelengths, feature symmetry changed, and spectral contrast first increased and then decreased. Finally, Mustard and Hays (1997) successfully used a combination of Mie theory (Conel, 1969) and a Hapke model (Hapke, 1993) to calculate spectra that matched the observed relationships, demonstrating that such modeling could be used to separate the effects of particle size and composition in spectra of fine particulate minerals.

2.7. *Effects of spectral resolution on determination of composition from olivine spectra*

Koeppen and Hamilton (2008) described the effect of reduced spectral resolution on the ability to distinguish between olivine solid solution compositions in mixtures, as well as on the development of long wavelength spectral indices used to identify olivine-related spectral features in emissivity spectra of the Martian surface. (Spectral indices reduce a key spectral feature such as a band minimum or maximum to a numeric value indicating the presence and relative strength of that feature.) Their analysis showed that for the suite of olivine emissivity spectra presented here, shifts in band position that are apparent in 4 cm^{-1} (laboratory) resolution spectra are not always resolvable at the 20 cm^{-1} resolution of the Mars Global Surveyor Thermal Emission Spectrometer (Christensen et al., 2001). They determined that long wavelength features used for spectral indices could not be distinguished for the following groups of compositions: $\mathrm{Fo}_{60,68}$, $\mathrm{Fo}_{25,35,39}$, and $\mathrm{Fo}_{1,10}$. Because the olivine emissivity spectra presented in Section 2.5 may be used for the interpretation of remote-sensing data acquired at reduced spectral resolution, a more detailed review of the effect of reduced spectral resolution on olivine band positions may be useful.

Fig. 15 shows the positions of Bands 1–12 in Mg–Fe olivine emissivity spectra at 20 cm^{-1} resolution (comparable to several Thermal Emission Spectrometers flown to Mars). I have plotted these in two frames to enable better visualization of the band positions. For every band, the reduction in resolution leads to

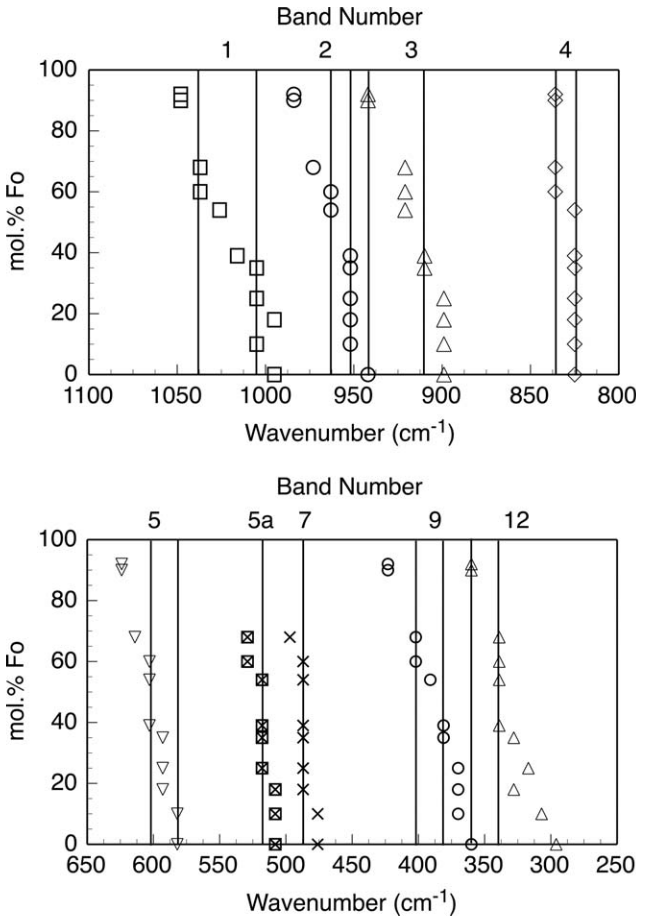

Fig. 15. Positions of emissivity minima in 11 natural olivines versus mol% forsterite at reduced spectral resolution (20 cm^{-1}). Vertical lines are for visual reference, and indicate band positions shared by more than one olivine solid solution composition. Band numbers (with the exception of 5a) defined by Burns and Huggins (1972) are shown at the top of each plot.

spectra with differing solid solution compositions having identically located band minima, which means that single bands cannot be used as effective discriminators of composition, in some cases, over wide ranges of composition. As one might predict, bands for which the compositional series exhibits a relatively large range of positions (shallower linear slopes in Fig. 10) at 4 cm^{-1} resolution (e.g., Bands 1, 3, 9, and 12) show a broader range of band positions at reduced resolution. For example, Band 3 position allows the discrimination of four compositional groups: $Fo_{0–25}$, $Fo_{35–39}$, $Fo_{54–68}$, and $Fo_{90–92}$. These specific groupings are, of course, dependent on the compositions represented by this particular suite of spectra at the measured spectral resolution and signal-to-noise; other combinations of these parameters may produce different results. Bands for which the compositional series exhibits a relatively narrow range of positions (steeper linear slopes in Fig. 10) at 4 cm^{-1} resolution (e.g., Bands 4 and 7) show little variation in band position across the range of Mg–Fe compositions at 20 cm^{-1} resolution. For example, at this resolution, Band 4 only allows the classification of unknown spectra into one of two groups: $Fo_{0–54}$ and $Fo_{60–92}$. In yet another situation, Bands 5a and 7 are relatively weak shoulders in forsteritic samples at 4 cm^{-1} resolution, and the reduction of resolution to 20 cm^{-1} makes these features very difficult to discern, and it is not possible to retrieve their positions. However, the lack of these features at low resolution might be used to infer a forsteritic composition, particularly if other band positions can be identified and are in the proper general locations for Mg-rich olivine.

In summary, band positions obtained from low spectral resolution data will yield predicted compositions with higher uncertainties if they are used as inputs to regression equations derived from laboratory-resolution data. Comparisons of the predicted compositions from multiple bands likely will give the most robust estimate of olivine composition. Although I have not discussed them in detail here, consideration of signal-to-noise and mineralogic mixtures are important to the proper comparative or quantitative analysis of remotely acquired infrared spectra. Remote-sensing data generally have lower SNR than laboratory spectra; the increased noise in remote-sensing data may make it harder to determine the exact position of a band minimum, leading to greater uncertainty in the predicted composition even if the spectral resolution is comparable to that obtained in the laboratory. Second, it is unlikely that many planetary surfaces are monomineralic; because mineral spectra add linearly in the infrared, spectral features of olivine on a planetary surface can be distorted by the contributions of other phases that are present. This makes qualitative analyses that rely on specific band positions (e.g., band indices) susceptible, at best, to greater uncertainties, and at worst, to misinterpretation. The most reliable analytical approach is one that verifies the presence of the majority of diagnostic bands (rather than one or a few), and the positions of those bands should all be consistent with a similar Mg–Fe ratio. This sort of analysis can be enhanced and/or enabled by the use of data manipulations that isolate spectral components of interest, such as carefully constructed spectral subtractions or ratios (e.g., Ruff and Christensen, 2002; Hamilton et al., 2003; Hoefen et al., 2003; Koeppen and Hamilton, 2008).

3. Identification of Mg–Fe olivines in planetary materials using TIR spectroscopy

Samples returned from planetary bodies provide an opportunity to measure in situ materials that normally are measured remotely. Lunar samples returned by the Apollo 11, 12, 14, and 15 missions were first analyzed in the TIR by Estep et al. (1971, 1972), who obtained transmission spectra of mineral separates and single mineral grains. The Mg–Fe compositions of olivines in the Apollo 11 and 12 olivine separates were constrained to $Fo_{72–66}$ using a cation determinative curve for Band 9, which varied in position between 401 and 397 cm^{-1} (Estep et al., 1971). Subsequent micro-IR analysis of these olivines as single grains showed that the compositional range indicated by the position of Band 9 was slightly broader, $Fo_{74–62}$, and that the inclusion of olivines from Apollo missions 14 and 15 broadened the total range further, to $Fo_{86–55}$ (Estep et al., 1972). Lunar reference suites from Apollo missions 12, 14, and 16 (Fischer, 1995) were measured in reflectance by Salisbury et al. (1997), who observed spectral differences in the ~1250–830 cm^{-1} region that they attributed to differing olivine abundances between samples in the Apollo 16a reference suite (representing dominantly friable light matrix breccia) and the Apollo 16b reference suite (highlands soils). Reduction of the strength of a reflectance peak near 925 cm^{-1} in Apollo 14 spectra was cited as evidence for a greater abundance of olivine in the Apollo 16b samples. In another example of the analysis of returned samples, Keller et al. (2006) measured thermal infrared spectra of materials collected by the Stardust mission from the comet 81P/Wild 2. Rare particles exhibit TIR features consistent with crystalline silicates, including olivine. The composition of olivine in one olivine-rich particle was constrained by the observation that the spectrum lacks the strong 33 μm feature (Band 13) typically present in the more Mg-rich olivines, and is estimated to be ~Fo_{75}. Many interplanetary dust particles (IDPs) collected in the stratosphere show transmission features characteristic of olivines in the Mg–Fe series (e.g., Sandford and Walker, 1985).

Acquisition of thermal IR spectra of geologic materials allows not just the identification of mineral composition in bulk materials and mineral separates from returned materials, but also permits the development of spectral libraries for comparison to data acquired of remote planetary surfaces, where the specific origins of the materials (e.g., meteorites, cometary dust) may not be known a priori. These comparisons can lead to the identification of mineralogy on remote surfaces, as well as the identification of a meteorite's parent body. Several studies have examined the thermal infrared signatures of meteorites via transmission spectroscopy (e.g., Zaikowski and Knacke, 1975; Sandford, 1984, 1993), although most of these have not attempted to identify the cation compositions of included phases. One of the earliest studies of a wide range of meteorite samples found that the transmission spectra of CO and CV carbonaceous chondrites, which have large abundances of olivine, are dominated by the spectral features of olivine, whereas spectra of ordinary chondrites exhibit a discernible shift in spectral character as the olivine to pyroxene ratio changes between LL, L, and H chondrites (Sandford, 1984). Sandford (1993) measured transmission spectra of seven Antarctic ureilites, which are shocked achondritic breccias known to contain abundant olivine ranging in composition from Fo_{97} to Fo_{76} (e.g., Takeda, 1991; Goodrich, 1992). Major features in the ureilite spectra were assigned to pyroxene and olivine by comparison to spectra of a series of standards of these phases having a range of cation compositions. Of 14 bands described, seven are attributed in whole or in part to olivine, with five of the seven described as being either Mg- or Fe-rich, presumably on the basis of the band positions, although this is not described in detail.

Several studies have examined thermal IR reflectance spectra of meteorites (Miyamoto, 1986, 1987; Salisbury et al., 1991a; Miyamoto and Zolensky, 1994). A large study of the reflectance spectra of 50 powdered (generally < 75 μm) stony meteorites has shown that the most prominent reststrahlen features are attributable to olivine and pyroxene, and that the relative strengths of olivine and pyroxene features are approximations of their relative abundance, i.e., they follow a linear mixing model (Salisbury et al., 1991a). Salisbury et al. (1991a) also discuss the presence of features in the ~2220–1330 cm^{-1} (4.5–7.5 μm) region of meteorite spectra that they attribute to overtone/combination tone bands in olivine and pyroxene. These authors go on to show that a doublet in olivine, at ~1820–1540 cm^{-1} (5.5–6.5 μm), becomes more prominent as the abundance of olivine increases, and that the feature positions move to longer wavelengths as heavier cations are substituted into the olivine (e.g., Fe for Mg). Fig. 16 shows inverted reflectance spectra (1200–400 cm^{-1}) of two olivine-bearing carbonaceous chondrites (Murchison and Ornans), an ordinary chondrite (La Criolla), a Martian meteorite (ALH A77005), a ureilite (Dingo Pup Donga), and the spectrum of an intermediate olivine (Salisbury et al., 1991a). Features of varying strength attributable to olivine are visible in the meteorites' spectra. Reflectance and emissivity spectra of the Martian meteorite NWA 2737 (Pieters et al., 2008), a dunite comprised primarily of brown olivine (Fo_{78}) containing a small amount of Fe^{3+}, show that the olivine in the meteorite is fully crystalline and its spectral shape is broadly similar to the spectrum of the Martian dunite meteorite Chassigny (Hamilton et al., 2003) and a forsteritic olivine, although the features in the meteorite are shifted to slightly lower wavenumbers than in the forsteritic olivine because the latter contains more magnesium.

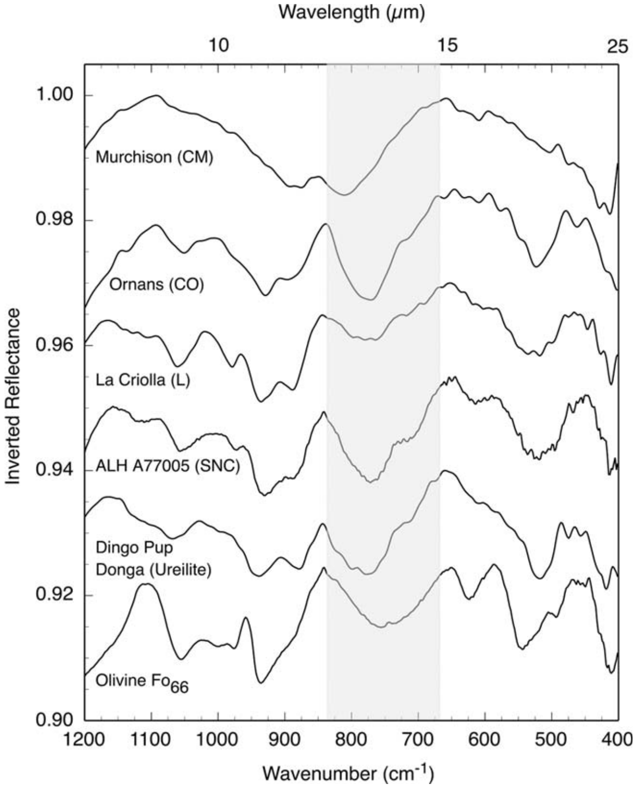

Fig. 16. Inverted reflectance spectra of olivine-bearing meteorites and an intermediate olivine (Salisbury et al. 1991a, b). Spectra are offset for clarity. Features in the gray shaded area are transparency features that result from volume scattering in fine particulate (< 75 μm) samples. Some meteorite spectra exhibit Christiansen features at higher wavenumbers than that observed in olivine because additional phases are present.

Numerical models that reproduce measured thermal IR spectra can provide an assessment of the modal mineralogy and mineral chemistry of planetary materials. Hamilton et al. (1997) measured emissivity spectra of solid samples of four Martian meteorites (two of which are olivine-bearing—Nakhla and ALH A77005) and used a linear least squares "deconvolution" model to identify the major phase compositions and their abundances. Linear least squares models are based on the principal that the thermal infrared spectra of geologic phases add linearly in proportion to their abundance (Lyon et al., 1959; Omori, 1967; Thomson and Salisbury, 1993; Ramsey and Christensen, 1998), and take as inputs the spectra of unknown materials to be modeled, a library of spectra of known materials (e.g., rock-forming minerals), and a wavenumber region over which the model should fit the spectra of the unknown materials. The algorithm performs a linear matrix inversion, using the spectral library to generate a best fit model spectrum, returns the phases used in the best fit and their abundances, and calculates the root-mean-square error and/or the covariances as an assessment of the quality of the fit (Ramsey and Christensen, 1998; Staid et al., 2004; Rogers and Aharonson, 2008). Fit quality is necessarily influenced by which phases are represented by the spectra in the library. If a major phase in the unknown is not represented in the spectral library, the phase cannot be identified, and the "best fit" spectrum may, in practice, demonstrate a poor fit. Hamilton et al. (1997) modeled the four meteorite spectra using a library of 11 mineral spectra (two orthopyroxenes, three high Ca clinopyroxenes, three plagioclase feldspars, two olivines—forsterite and fayalite, and a shocked feldspar (maskelynite)), and found that for Nakhla, the modeled olivine abundances were within the range of values measured by other methods, and that in the case of ALH A77005, the modeled abundance was within 2% of the measured mode. Olivine in Nakhla is ~Fo_{32} (Berkley et al., 1980), and the fayalite library spectrum was used in the best fit. Olivine in ALH

Please cite this article as: Hamilton, V.E., (2010), doi:10.1016/j.chemer.2009.12.005

A77005 is intermediate to Mg-rich, ~Fo_{74} (McSween et al., 1979), and the modeled fit used both the forsterite and fayalite library spectra in the best fit, with roughly twice as much forsterite as fayalite. Despite the reasonably good modeled mineralogies for these two samples, the roughly linear shift in olivine spectral features with Mg:Fe means that spectra of intermediate compositions cannot be as well modeled by a linear mixture of the spectra of forsterite and fayalite as they can be if spectra of intermediate compositions are available; an example of this was revealed in the analysis of Martian remote sensing data described below in Section 4, and the models of several of these meteorite spectra are revisited in Section 5 with an updated spectral library containing intermediate olivine compositions.

Microspectroscopy is a means of obtaining the TIR spectra of planetary dusts, micrometeorites, phases that are sufficiently small that it is impractical to attempt to separate them from their host rock or particle, etc. (e.g., Raynal et al., 2000; Osawa et al., 2001; Bradley, 2004; Morlok et al., 2006a, 2006b). For example, microscopic TIR spectroscopy has been used in the classification of chondritic IDPs, establishing that there are three primary classes, one of which is dominated by olivine (c.f., Bradley, 2004). Osawa et al. (2001) demonstrated that the spectra of Antarctic micrometeorites contain features attributable to olivine. Morlok et al. (2006b) separated olivine grains (Fo_{60-100}) from primitive meteorites, measured their thermal IR spectra from 5000 to 625 cm^{-1} (2–16 μm), and recorded the positions of five bands as a function of Mg–Fe ratio. These authors have adopted a band ordering that is the reverse of that described in the majority of the literature, numbering their Bands 1–5, where these represent features at ~833, 893, 962, 990, and 1000 cm^{-1} (~12.0, 11.2, 10.4, 10.1, and 10.0 μm), respectively. Bands 1–3 and 5 in Morlok et al. (2006b) correspond to Bands 4, 3, 2, and 1, respectively, in Section 2; to maintain consistency with the literature described in Section 2, I will refer to peak locations in wavenumber and use the band numbers defined by Burns and Huggins (1972). Morlok et al. (2006b) point out that the features they observe at 990 and 1000 cm^{-1} are not distinguished as separate bands in some of the studies described in Section 2, which they attribute to the similar strengths of the two features and the closeness of their peak positions. As with prior studies, the observed trends in band position as a function of Mg:Fe are found to be linear, and the fits to Bands 3 and 4 (833 and 893 cm^{-1}) are nearly the same as for terrestrial olivines examined in prior studies, despite the fact that the olivines examined by Morlok et al. (2006b) are limited to Fo_{60-100}. The feature at 962 cm^{-1}, however, displays a steeper slope in the meteoritic olivines than in the terrestrial olivines. The authors attribute this difference to the narrower Fo range represented by their samples' spectra and suggest that the slope is shallower at lower $Fo_{\#}$ ($<Fo_{60}$), and that the entire range of the terrestrial data for Band 2 is better fit by a quadratic equation (the correlation coefficients are not given, so the degree of improvement is not stated). Finally, the authors suggest that the spectral resolution of astronomical spectra is too low to allow derivation of Mg:Fe in olivines, but their discussion is not explicit as to what combination of resolution and signal-to-noise would be required to estimate Mg:Fe.

4. Identification of Mg–Fe olivines on planetary surfaces using TIR spectroscopy

Excluding Earth, where we can examine olivine-bearing rocks firsthand in most cases, the planetary surfaces in our solar system most likely to exhibit olivine signatures in the thermal infrared are Mercury, Venus, Earth's Moon, Mars, asteroids, and satellites of the outer solar system planets (comets are not considered here because most observations are of their comae, not surfaces). Although chemical evidence collected by several Soviet Venera and Vega landers in the 1970s and 1980s suggested the rock types on Venus are consistent with olivine-bearing lithologies (Fegley et al., 1997), the surface of Venus is obscured at thermal infrared wavelengths by a dense cover of clouds comprised of sulfuric acid and water vapor (Donahue and Russell, 1997). The surfaces of satellites of the outer planets do not appear to exhibit any definitive TIR signatures. Analysis of thermal infrared spectra acquired of Saturn's moons Phoebe, Iapetus, Enceladus, Tethys, and Hyperion suggests that they lack TIR features because the surfaces are likely to be comprised of materials with small particle sizes and large porosity (Carvano et al., 2007). Similarly, no features of silicates have been observed on the Galilean satellites Europa and Callisto (Mills and Brown, 2000). Among the remaining bodies, TIR spectra of Mercury, Mars, the Moon, and some asteroids exhibit features that have been suggested to be consistent with materials bearing Mg–Fe olivine phases—these are summarized below. Although Mn- and Ca-bearing olivines are not a subject of this review, it is worth noting that I have not encountered any claims in the peer-reviewed literature for the identification of olivines having these compositions on extraterrestrial surfaces.

4.1. Mercury

Visually, Mercury resembles Earth's Moon, exhibiting a heavily cratered surface with modest features of extrusive volcanism (e.g., Head et al., 2008; Murchie et al., 2008), but otherwise relatively bereft of features indicative of long-term geologic activity like that observed on Earth. The surface of Mercury has not been studied up close in the thermal infrared by orbital or landed spacecraft, so obtaining TIR spectra of the surface of Mercury has only been accomplished using ground-based telescopes or airborne instruments capable of getting above much of the Earth's atmosphere, and then only for certain locations on the planet's surface. Interpretation of Mercurian infrared spectra is challenging as a result of the vacuum environment and low thermal inertia (likely indicating fine particle sizes) of the surface materials (Chase et al., 1976). Although there have been indications of feldspathic and possibly pyroxene mineralogies from thermal IR spectra of the Mercurian surface (e.g., Emery et al., 1998; Sprague et al., 2000, 2002), only recently has there been any suggestion of possible olivine features. Sprague et al. (2009) acquired thermal IR spectra covering the range from ~8 to 12.7 μm for three locations on Mercury: the radar bright region C, the dark plains west of the Caloris Basin, and the Caloris Basin interior. These researchers' linear least squares models of their spectra suggest that Mg-olivine is present only in the radar bright region C. For the spectrum of this area, 10 permutations of the spectral model were run, identifying Mg-olivine at abundances ranging from 0% to 37%, which is proposed to be contained in oligoclase basalt (Sprague et al., 2009). However, the authors do not discuss mineral detection limits based on the spectral resolution and signal-to-noise of their data, or include in their quantitative analysis the effects of thermal gradients on spectra of particulates measured in vacuum, two factors that make it difficult to ascertain the confidence with which one should view the precision and accuracy of the reported abundances. At present, it is possible that olivine has been identified in the radar bright region C on Mercury, but it is probably premature to quote specific abundances. The Bepi-Columbo mission, scheduled for launch in 2014 will carry the first thermal infrared imaging spectrometer (Helbert et al., 2005) to map the surface Mercury from orbit and should enable a more detailed evaluation of potentially olivine-bearing surfaces.

4.2. The Moon

Like Mercury, thermal infrared spectroscopy of Earth's Moon is complicated by the vacuum environment and fine particle sizes of the materials. As a result, there has been controversy in the literature as to the utility of TIR spectroscopy for the determination of lunar surface composition. This is in part due to variable quality of the observations, and partially attributable to the data being analyzed in the time period prior to and during which the first thorough laboratory examinations of appropriate analogues were undertaken in simulated lunar environments (e.g., Goetz, 1968; Murcray et al., 1970; Salisbury et al., 1970; Tyler et al., 1988; Nash et al., 1993). Nash et al. (1993) provide an excellent review of this literature and demonstrate why thermal infrared spectroscopy of the lunar surface should be pursued. Nonetheless, although some investigators have identified what they interpreted as diagnostic emissivity features of olivine in lunar spectra, these results have been called into question. Ground-based measurements by Sprague et al. (1992) suggest that the central peak of the crater Copernicus exhibits a Christiansen feature peak location characteristic of mafic materials and an emission minimum at 952 cm^{-1} (10.5 μm) consistent with the laboratory spectrum of forsteritic olivine. Salisbury et al. (1995) compared the ground-based lunar spectra of Sprague et al. (1992) to thermal IR laboratory spectra of returned lunar samples and argued that the high-frequency structure and spectral contrast of the ground-based lunar spectra are inconsistent with the broader spectral features and lower spectral contrast of the reststrahlen features in laboratory spectra of lunar samples. Salisbury et al. (1995) therefore concluded that the features in the Sprague et al. (1992) spectra are largely attributable to artifacts. The Diviner radiometer onboard the Lunar Reconnaissance Orbiter (Paige et al., 2009) is measuring reflected and emitted radiation from the lunar surface and provides multispectral data that are free of the complicating effects of the terrestrial environment; hopefully these data will enable additional constraints on the composition of the lunar surface, and inferences about the presence or absence of olivine as a function of location.

4.3. Mars

Interpretation of Martian thermal IR surface spectra is simplified relative to other planetary bodies as a result of the modest atmospheric pressure, which substantially reduces thermal gradients (Henderson and Jakosky, 1994, 1997), and the presence of large surface areas having sufficiently high thermal inertia to infer that they represent materials in the form of coarse particulates to near-bedrock, which eliminates particle size effects (e.g., Christensen, 1982; Presley and Christensen, 1997; Mellon et al., 2000; Putzig et al., 2005). Although the Martian atmosphere contains silicate dust, this component essentially adds linearly with the surface spectrum and can be separated from the surface component (e.g., Smith et al., 2000).

Surface compositions on Mars, like Mercury, can be derived from thermal emission spectra by the application of a linear least squares fitting algorithm. To interpret Martian spectra, spectra of atmospheric components are included in the spectral library used to fit the data, and their fractional contribution is subtracted to obtain the surface spectrum and modeled surface mineralogy. Details of detection limits and analytical accuracy and precision associated with Martian spectral modeling can be found in the literature cited in this section, but in general for the data discussed here, detections >5–10% are considered believable with absolute values conservatively reliable to about 5%. Using this analytical approach, thermal infrared spectra collected by the thermal emission spectrometer (TES) onboard the Mars Global Surveyor spacecraft first revealed the complete major phase mineralogy of the basaltic component of the Martian surface (Bandfield et al., 2000), including modest abundances (~10–15%) of olivine (Christensen et al., 2000a).

Subsequently, regions with even greater abundances (up to 30%) of olivine in basalt, interpreted as representing compositions ranging from ~Fo_{30-70}, were identified using the linear least squares modeling approach as well as by direct comparisons of spectral features in the Martian spectra with band positions in laboratory spectra of olivines (Hamilton et al., 2003; Hoefen et al., 2003). One of the largest regions containing olivine-enriched materials, near grabens referred to as the Nili Fossae, has an area of over 113,000 km^2 (Hamilton and Christensen, 2005). These materials have been hypothesized to originate from exposed intrusions (Hoefen et al., 2003), laterally extensive lava flows (Hamilton and Christensen, 2005) or an impact melt sheet (Mustard et al., 2007). In another case, in and near the canyon system of the Valles Marineris, thermal infrared images from the Thermal Emission Imaging System (THEMIS) onboard the 2001 Mars Odyssey spacecraft revealed a series of outcrops forming an apparently continuous unit of olivine-enriched basalts stretching laterally for more than 1100 km and having an estimated volume of $\sim 9.9 \times 10^4$ km^3 (Edwards et al., 2008). Several hypotheses for the origin of these materials have been suggested, but Edwards et al. (2008) favor a scenario where they represent a relatively discrete period in Martian history when flood lavas were erupted, suggesting that these are picritic basalts derived from primitive magmas.

Several studies have examined the global distribution and compositional variation of olivine on Mars using orbital TIR data. Early results by Bandfield (2002) suggested that olivine was not globally prevalent; this was because his mineral maps, produced using the linear least squares approach with a library containing only forsterite and fayalite spectra, did not reveal a widespread distribution of olivine. However, as emissivity spectra of intermediate compositions and olivine-bearing Martian meteorites became available, a different picture of the distribution of olivine on Mars began to emerge. Hamilton et al. (2003) attempted to identify candidate Martian meteorite source regions by modeling TES spectra using a library containing laboratory spectra of Martian meteorites and the dominant TES Martian surface and atmospheric spectra; they found numerous locations around the planet where components of the Martian spectra matched the signatures of the meteorites Chassigny and ALH A77005, where Chassigny contains ~90% Fo_{68} (Prinz et al., 1974), and ALH A77005 contains ~44–60% of ~Fo_{74} (e.g., McSween et al., 1979; Mason, 1981; Treiman et al., 1994). McSween et al. (2006) mapped the global distribution of olivine using a model that included spectra of a few compositions intermediate to forsterite and fayalite, showing that olivine is widespread on Mars, with the relatively older equatorial and southern highlands regions typically containing abundances up to 20%, whereas the relatively recently resurfaced northern lowlands are largely devoid of olivine. Koeppen and Hamilton (2008) advanced global mapping of olivine further, using the linear least squares model approach with a library containing six olivines (Fo_{91}, Fo_{68}, Fo_{53}, Fo_{39}, Fo_{18}, and Fo_1) and producing maps of the distributions of each of these compositions (where each map represents a range of approximately plus and minus 10 mol% forsterite around the specified value; a similar range applies to the forsterite compositions and ranges referred to throughout the remainder of this paragraph). Their model-derived results were supported by detailed examination of individual spectra (Fig. 17) and the mapping of olivine spectral feature indices. Koeppen and Hamilton (2008) found that the spatially and fractionally dominant solid solution composition of olivine on Mars is around Fo_{68}, consistent with expectations based on Martian meteorite olivine compositions, with the next most abundant compositions ranging

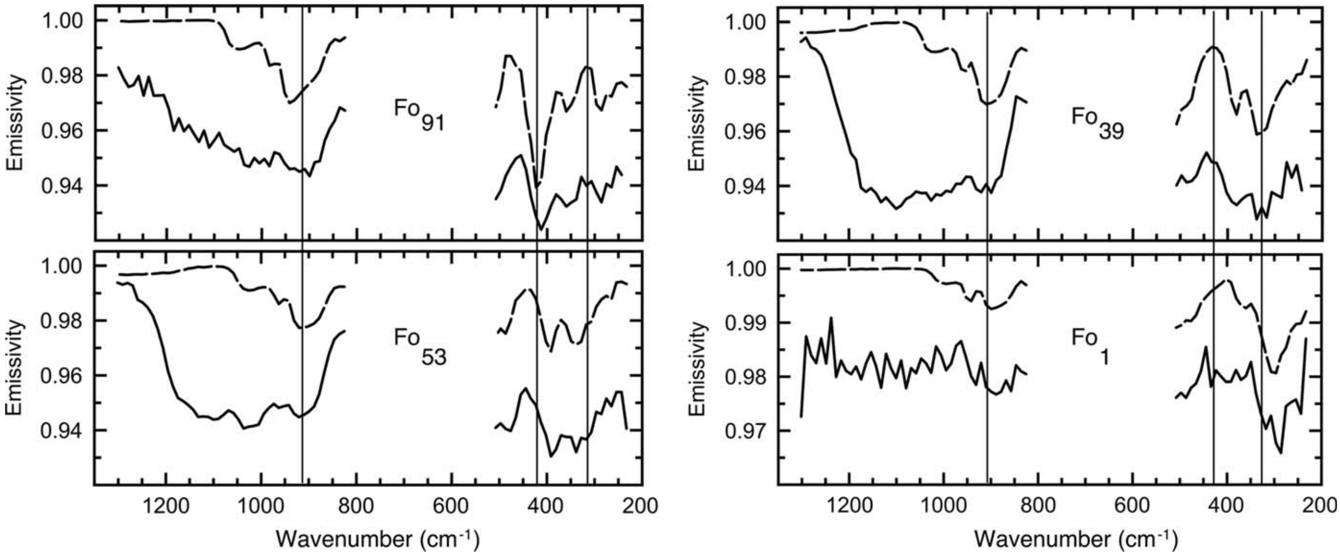

Fig. 17. Emissivity spectra of olivine-bearing basaltic surfaces on Mars (solid lines) compared to pure olivine spectra (dashed lines) at similar spectral contrast. Martian surface spectra have been corrected to remove atmospheric dust and the gap between ~800 and 500 cm^{-1} represents a region where the surface is obscured by gaseous CO_2 in the Martian atmosphere. Vertical lines are for visual reference and denote minima or peaks in one of the panels. After Koeppen and Hamilton (2008).

from Fo_{53-39}, considerably more Fe-rich than observed in most Martian meteorites. Although they are not globally common, detailed examination of TES spectra confirmed the presence of basaltic materials containing olivine with compositions as Mg-rich as Fo_{91} and provided equivocal evidence for compositions as Fe-rich as Fo_{18-1} (Fig. 17). The most magnesian olivine-bearing materials are restricted to ancient terrains adjacent to large impact basins and may represent primitive mantle material, whereas intermediate and more Fe-rich olivines occur in basaltic materials spanning Martian history. Regional studies of TIR spectra support these global results, and can more readily incorporate local geologic context into interpretations of the origins of olivine-bearing basalts on Mars (e.g., Rogers et al., 2005; Edwards et al., 2008; Tornabene et al., 2008).

In situ thermal infrared measurements by the Mars Exploration Rovers *Spirit* and *Opportunity* support the orbital identification of olivine on Mars and extend it to locations not readily observed from orbit due to dust on the surface (Christensen et al., 2004b, 2004a; Ruff et al., 2006). At the landing site of the rover *Spirit* in Gusev crater, olivine of intermediate composition (Fo_{35-60}) is present at abundances up to 20–30% in picritic basalt rocks that bear similarities to some Martian meteorites (Christensen et al., 2004b; McSween et al., 2006; Ruff et al., 2006). At *Opportunity*'s landing site in Meridiani Planum, olivine having a composition near Fo_{60} was identified in basaltic sands at typical abundances of up to 15%; these soils, corrected to remove secondary phases, have basaltic compositions similar to those identified from orbit (Christensen et al., 2004a; Glotch and Bandfield, 2006; Rogers and Aharonson, 2008). These olivine-bearing sands may have been transported to their current location from elsewhere, as there are no apparent parent outcrops in the vicinity, but the presence and prevalence of olivine in the TIR signatures of these rocks has been used to argue that there have been long periods of relatively dry conditions, as olivine is expected to be highly susceptible to chemical weathering in the presence of water (e.g., Christensen et al., 2004a; Glotch and Bandfield, 2006; Rogers and Aharonson, 2008).

4.4. Asteroids

Although thermal infrared measurements of asteroids and comets have been made for upwards of 35 years, primarily with the objectives of constraining diameters and albedos (e.g., Price, 2002), thermal emission spectroscopy has a relatively short history of being used to study the compositions of asteroids and comets. Many studies (e.g., Cohen et al., 1998; Heras et al., 2000; Barucci et al., 2002; Dotto et al., 2002, 2004; Stansberry et al., 2004; Lim et al., 2005; Emery et al., 2006; Gehrz et al., 2006; Lisse et al., 2006; Barucci et al., 2008) have identified spectral features proposed to be indicative of physical characteristics, such as particle size and porosity, as well as composition, including the presence of olivine. Heras et al. (2000) suggested that the positions of features in the thermal IR spectrum of asteroid 4 Vesta are consistent with the positions of olivine features observed in the mass absorption coefficients determined from olivine transmission spectra acquired by Jäger et al. (1998). However, the features in the spectrum of 4 Vesta are unusually narrow for a silicate-dominated lithology, and recall the arguments of Salisbury et al. (1995) with respect to lunar surface spectra, where similarly narrow features were suggested to be artifacts. Dotto et al. (2000) observed five Main Belt asteroids (1 Ceres, 2 Pallas, 3 Juno, 4 Vesta, and 52 Europa) with the Infrared Space Observatory (ISO) and compared their infrared spectra to the laboratory spectra of several minerals, including a forsteritic olivine. These investigators found spectral similarities between features in olivine and those in the spectra of 3 Juno, 4 Vesta, and 52 Europa. In the case of 3 Juno, the position of the Christiansen feature at ~1160 cm^{-1} (~8.6 μm) is suggested to be due to a mixture of pyroxenes and olivines, as is the spectral shape between 1250 and 910 cm^{-1} (8–11 μm) in the spectrum of 52 Europa. The spectral peak at 1136 cm^{-1} (8.8 μm) in 52 Europa's spectrum also is proposed to be consistent with olivine. Spectral structure around 1100 cm^{-1} (9.1 μm) in the spectrum of 4 Vesta is interpreted as related to an olivine component.

Several studies have identified qualitative similarities between asteroid thermal IR spectra and the laboratory spectra of certain meteorites (carbonaceous chondrites, diogenites) that typically contain Mg–Fe olivine and permit the inference that olivine may be present, even if specific features are difficult to observe. Using spectra acquired by ISO, Dotto et al. (2002) found broad spectral shape similarities between 114 Kassandra and 308 Polyxo and the meteorite Ornans (CO3) at a particle size fraction of <20 μm; they also described broad similarities between the spectrum of 511 Davida and Murchison (CM) (see Fig. 16 for example spectra of Ornans and Murchison). Subsequent ISO observations of 308 Polyxo by Dotto et al. (2004) were also deemed to be consistent with the spectrum of Ornans. Observations of 10 Hygiea by Barucci et al. (2002) using ISO were best matched by spectra of fine particulate fractions of Ornans and Warrenton (CO3). The Rosetta spacecraft flew past asteroid 2867 Steins on 5 September 2008 and is scheduled to fly by 21 Lutetia in June 2010. Barucci et al. (2008) acquired thermal IR spectra of both targets using the Spitzer Space Telescope, and found spectral similarities between Steins and enstatite achondrites and between 21 Lutetia and fine particulate Ornans and Vigarano (CV), suggesting that 21 Lutetia may be partially comprised of olivine. A study of the TIR spectra of 29 asteroids by Lim et al. (2005) found that the majority of asteroids lacked spectral features (likely due to fine particulate regoliths), and in some cases, they were not able to confirm the results of prior investigators who observed spectral features interpreted as indicative of composition (e.g., in 2 Pallas, 4 Vesta, and 10 Hygiea). In their study, Lim et al. (2005) found that only 1 Ceres and 4 Vesta exhibited spectral contrast as large as 2–5%. In the case of 4 Vesta, Lim and coworkers did not attempt a detailed mineralogical analysis, citing low spectral contrast, but observed that laboratory spectra of howardite, eucrite, and diogenite (HED) meteorites exhibit some of the features observed in the spectrum of the asteroid. Among the HED meteorites, diogenites contain small amounts of olivine, but it is likely inappropriate to infer the presence of olivine on 4 Vesta from these spectra.

Spitzer Space Telescope observations of three Trojan asteroids (624 Hektor, 911 Agamemnon, and 1172 Aneas) were studied by Emery et al. (2006), who observed strong features and attempted, for the first time, to use a linear least squares model to determine the asteroids' compositions. The modeling effort was not successful, but Emery and coworkers found that the Trojans' infrared spectra bore greater similarity to the spectra of olivine-bearing cometary comae (e.g., Wooden et al., 1999; Stansberry et al., 2004; Lisse et al., 2006) than to laboratory spectra of minerals and meteorites. Because spectra of cometary comae represent emission from well separated particles, the spectra of the Trojans may represent surfaces with underdense, fairy castle-like structures (Hapke and van Horn, 1963) or silicates suspended in a transparent matrix in the asteroids' regoliths—materials for which good laboratory spectral analogues do not exist (Emery et al., 2006). Nonetheless, it may be possible to infer the presence of olivine on the Trojans' surfaces by comparison to the spectra of comae suggested to exhibit olivine features.

5. Linear least squares mixture analysis for determination of olivine abundance and solid solution composition

Most planetary materials are not composed of single phases, raising the question of how to distinguish various phases in mixtures and estimate their abundances. As described above in Section 3, the spectra of mixtures can be mathematically modeled relatively straightforwardly using a linear least squares approach to identify the major component phases and retrieve their abundances, typically to within about 5–10 vol% for laboratory quality (2 cm^{-1} sampling) data (Ramsey and Christensen, 1998; Hamilton and Christensen, 2000; Wyatt et al., 2001; Rogers and Aharonson, 2008). The phase percentages generally are reported as volume percent by analogy with thin section analyses, where an areal measurement is assumed to be representative of volume abundances. The uncertainties associated with the derived modal abundances vary with mineralogy, spectral resolution and range, and signal-to-noise, and should be established for each set of measurements that differs in these characteristics from previously published work.

Here I show linear least squares modeling results for five Martian meteorite emissivity spectra (EET A79001 lithology A, Nakhla, Lafayette, ALH A77005, and Chassigny), with the objective of demonstrating the fidelity with which the abundances of Mg–Fe olivines can be determined and their solid solution compositions constrained in mixture spectra. These meteorites represent basalt (EET A79001A), clinopyroxenite (Nakhla, Lafayette), basaltic lherzolite (ALH A77005), and dunite (Chassigny) lithologies having a range of olivine abundances and Mg–Fe solid solution compositions. This analysis improves upon an earlier analysis of a set of Martian meteorite emissivity spectra modeled by Hamilton et al. (1997) by updating the spectral library and using a slightly different linear least squares fitting algorithm. The original work by Hamilton and coworkers was the first peer-reviewed publication to use the linear least squares fitting method with natural lithologies, and the best practices for applying this analytical technique were still being developed. Relative to that study, which used only 12 library spectra to fit the spectra of the meteorites, it is now common practice to use a library containing several dozen spectra, including spectra representing alteration phases and a wide range of compositions within the most common primary solid solution series (e.g., plagioclase feldspars, clino- and orthopyroxenes, etc.) (e.g., Feely and Christensen, 1999; Bandfield et al., 2000; Hamilton and Christensen, 2000; Wyatt et al., 2001; Bandfield, 2002; Rogers et al., 2005; Dunn et al., 2007; Milam et al., 2007). Enhancements to the fitting algorithm permit a substantially larger library to be used and provide phase-specific assessments of the uncertainty associated with the model results; the algorithm I use here is that of Rogers and Aharonson (2008) and full details of the improvements represented by this algorithm can be found in their paper. In this analysis, the spectral library contains 75 spectra covering a broad range of common compositions in the feldspar, pyroxene, olivine, phyllosilicate, sulfate, zeolite, and oxide mineral groups, as well as several glasses. A discussion of the infrared emissivity spectra of these mineral groups is beyond the scope of this paper, but the spectra and discussions of their variations with solid solution composition can found in the literature (Piatek, 1997; Ruff, 1998, 2004; Christensen et al., 2000c; Hamilton, 2000; Michalski et al., 2003, 2006; Lane, 2007). The model was run over the range 1300–350 cm^{-1} two times, with the only difference being the number of olivine spectra included in the spectral library. In Model 1, I used the full spectral library, which contains all available olivine emissivity spectra in the range Fo_{90-0} (Table 5). In Model 2, I have removed all intermediate olivines so that only forsterite (Fo_{90}) and fayalite (Fo_0) are included to represent olivines. This model represents a case similar to two previously published studies where no intermediate olivines were available (Hamilton et al., 1997; Bandfield, 2002). The measured and modeled meteorite spectra are shown in Fig. 18. Table 8 lists the modal mineralogies of the meteorites by major mineral group (Meyer, 2003 and references therein), the value or range of mol% forsterite of olivine in each meteorite, and the model-derived mineral abundances and olivine solid solution compositions. A standard deviation (uncertainty) is given for each derived mineral group abundance. If more than one olivine spectrum is used in the best fit, the modeled mol% forsterite is derived by calculating the weighted average of the mol% forsterite represented by the spectra used in the best fit. This calculation allows for easy comparison to measured values, but assumes that a lithology contains only one olivine composition; for the Model 1 case, detailed examination of the olivine spectra used in the best fit may provide additional insight into the range of compositions that may be present if, for example, olivine crystals are zoned (the Model 2 case includes only forsterite and fayalite, and therefore must be interpreted in terms of the average composition). Fig. 18**a**

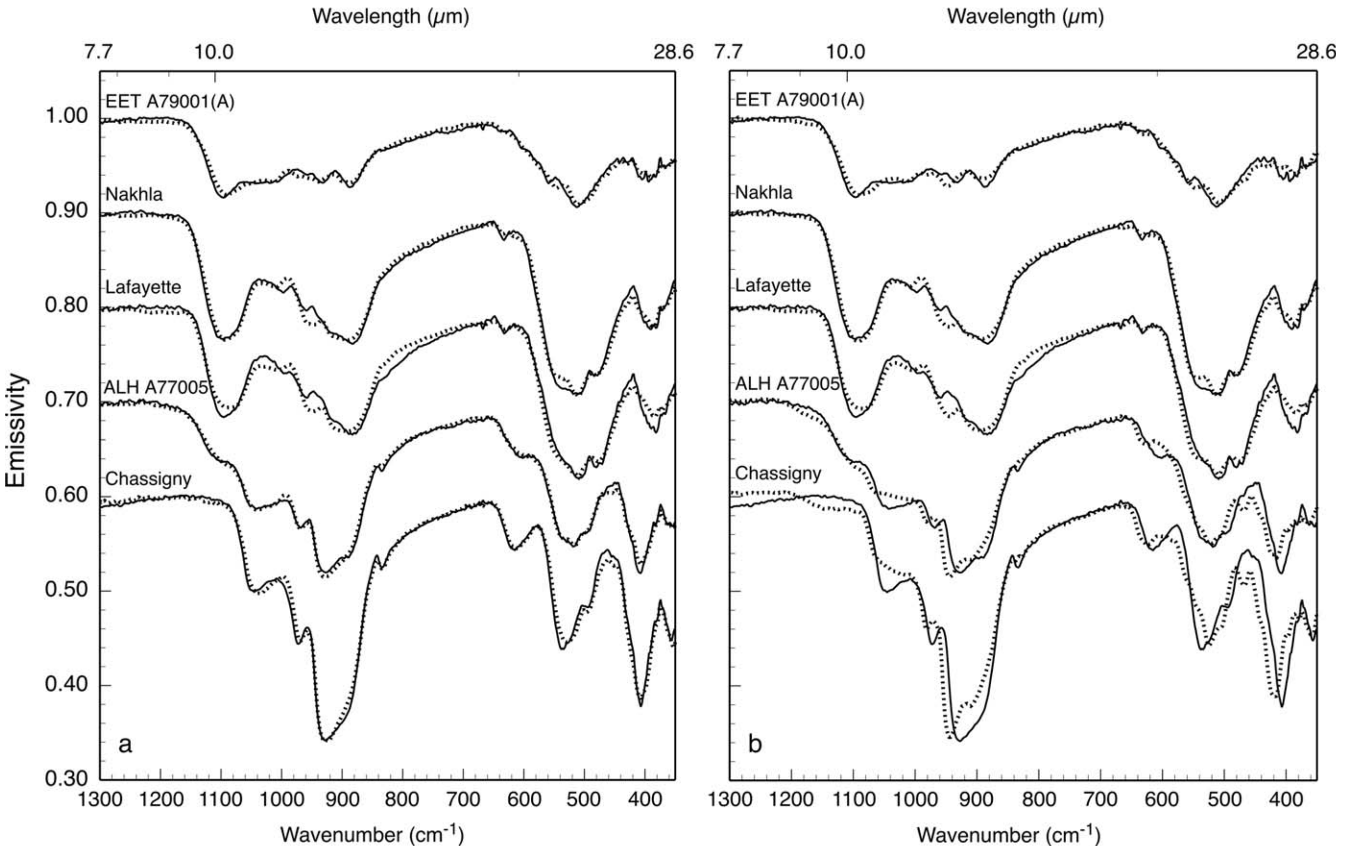

Fig. 18. Measured (solid lines) and modeled (dotted lines) spectra of olivine-bearing Martian meteorites. Modeled spectra in (a) were generated using a library that included olivine spectra representing a range of compositions from Fo_{91} to Fo_0, whereas modeled spectra in (b) were generated using a library with olivine spectra representing only Fo_{91} and Fo_0. Spectra are offset for clarity.

shows the measured and model-derived spectra for the first model (Mod1 in Table 8) and Fig. 18**b** shows the measured and model-derived spectra for the second model (Mod2 in Table 8). Below I describe details of the Model 1 and 2 fits, derived modal abundances, and derived olivine compositions for each meteorite in order of increasing olivine content in the meteorites.

The Model 1 fit to the spectrum of EET A79001(A) correctly determines that the lithology is pyroxene-dominated and contains olivine. The derived abundances of pyroxene and olivine are each slightly elevated by ~4–5 vol% relative to what has been observed in the meteorite. The model spectrum exhibits a minor misfit near 970 cm^{-1} (Fig. 18**a**) and plagioclase feldspar is not identified. Feldspar in EET A79001(A) has been shocked and converted to maskelynite, but this should not strongly affect the model results as the spectral library contains spectra of maskelynite (Hamilton et al., 1997) and two laboratory-shocked feldspars (Johnson, 2002). The more likely culprit for the minor misfit to the spectrum and the resulting errors in derived mineralogy is pigeonite, which comprises 40–63 vol% of the meteorite, and for which there is only one spectrum in the library, whereas the pigeonite in EET A79001(A) spans a broad range of compositions (c.f., Meyer, 2003). Pigeonite has more spectral structure than maskelynite, so the absence of an ideal-fitting pigeonite probably is accommodated by the use of additional pyroxene and olivine (minerals that have more spectral structure than maskelynite). Nonetheless, the fit is sufficiently good overall that we can compare the derived mol% forsterite ($Fo_{\#}$) in olivine to that which has been measured in the meteorite. The measured compositions range from Fo_{55-81}, and the modeled composition is Fo_{66}, well within the known values. Three olivine spectra were used in the best fit: Fo_{68}, Fo_{60}, and Fo_{54}, suggesting that a range of olivine compositions is present in the meteorite. The Model 2 derived spectrum also exhibits a misfit near 970 cm^{-1} (Fig. 18**b**) but identifies plagioclase at an abundance approaching that which has been observed in the meteorite. The model overestimates slightly the pyroxene abundance, but the derived olivine abundance is within the measured modes. The derived olivine composition in this model is Fo_{73}, which is also well within the range of known compositions.

Nakhla and Lafayette are both Nakhlites (clinopyroxenites) and have very similar mineralogies. Minor misfits are apparent in the modeled spectra of both meteorites around 945 cm^{-1} (Fig. 18**a**), and probably arise from slight differences between the spectral shapes of augites in the spectral library and in the meteorites, as augite is the modally dominant phase in both lithologies. The Model 1-derived mineral group abundances identify these as pyroxene-dominated lithologies, with modeled pyroxene abundances within the range of measured values. Plagioclase is rare in Nakhla (4 vol%) and is not identified in the fit. Plagioclase is not identified separately in Lafayette—but is included at 5 vol% in the model. Olivine is the second most abundant phase, and modeled abundances are within the range of known values (Table 8). Olivines in Nakhla range from Fo_{25} to Fo_{35} and cluster around Fo_{35} in Lafayette. The modeled values are Fo_{35} and Fo_{24}, respectively, with Nakhla being modeled using only the Fo_{35} library spectrum, and Lafayette being modeled by both Fo_{39} and Fo_{18}. In Model 2, the derived modal mineralogies are generally similar, with derived values near or within the range of known abundances, but the modeled olivine compositions are Fo_0 in both cases, clearly underestimating the magnesium

Please cite this article as: Hamilton, V.E., (2010), doi:10.1016/j.chemer.2009.12.005

Table 8
Measured and modeled modal abundances in Martian meteorites.

	EET A79001(A)					Nakhla					Lafayette					ALH A77005					Chassigny				
	Meas	*Mod1*	*Std.Dev.*	*Mod2*	*Std. Dev.*	*Meas*	*Mod1*	*Std. Dev.*	*Mod2*	*Std. Dev.*	*Meas*	*Mod1*	*Std.Dev.*	*Mod2*	*Std. Dev.*	*Meas*	*Mod1*	*Std. Dev.*	*Mod2*	*Std. Dev.*	*Meas*	*Mod1*	*Std. Dev.*	*Mod2*	*Std. Dev.*
Plagioclase	16–22	0	0	12	2.3	4	0	0	0	0	(incl. w/ other)	5	2.3	6	2.3	8–12	11	3	41	3.2	2	5	1.0	32	4.5
Pyroxene	61–74	79	1.1	80	1.9	74–85	82	1.4	89	1.7	70–84	73	1.7	76	1.8	13–43	25	1	23	2.8	5	0	0	1	1.2
Other	<5	7	1.4	3	1.4	3	9	0.9	8	1.2	9–11	5	0.6	5	0.7	5	19	3.1	4	2	<2	2	0.5	0	0
Olivine	3–10	15	0.6	5	1.1	5–18	9	1.2	3	1.1	8–20	16	1.4	12	1.3	44–60	45	0.5	31	1.5	92	93	1.1	68	2.6
Fo#[a]	55–81	66		73		25–35	35		0		35	24		0		70–75	66		59		68	69		60	

Meteorite data summarized from Meyer (2003), see references therein for original data. All abundances are rounded to the nearest integer and are approximate.

[a] Modeled $Fo_{\#}$s are the weighted average of the compositions used in the best fit.

content. Small misfits in the low wavenumber region of the spectra (e.g., around the peak at 420 cm^{-1} and the minimum around 380 cm^{-1} in Fig. 18**b**) are greater in the Model 2 spectra than in the Model 1 spectra, and likely are attributable to the lack of an olivine library spectrum with the correct composition and band positions. However, in broad terms, the olivine in these meteorites is iron-rich, and of the two library spectra available, the spectrum representing the iron-rich olivine provides the best fit.

ALH A77005 is an olivine-rich lithology, with 44–60 vol% olivine ranging in composition from Fo_{70} to Fo_{75}. Model 1 provides a very good spectral fit to the measured spectrum (Fig. 18**a**), matching band positions and amplitudes well, and the derived modes for the plagioclase, pyroxene, and olivine mineral groups are within the range of known modes. A slight excess of "other" phases is modeled relative to the measured 5 vol%; some of this can be accounted for within the uncertainty, and prior work has shown that small amounts of phases that may not be present may be included to minimize the RMS error (e.g., Ramsey and Christensen, 1998; Rogers and Aharonson, 2008). The modeled olivine is slightly more iron-rich (Fo_{66}) on average than the measured values (Fo_{70-75}); three olivines were used in the best fit: Fo_{91} (7 vol% of total olivine), Fo_{68} (91 vol%), and Fo_{10} (2 vol%). Instead of representing a broad range of olivine compositions in the meteorite, the distribution of compositions used in the best fit suggests that the olivine in the meteorite is close to Fo_{68}, but is more magnesium rich (represented by Fo_{91}) and not well represented by a single library composition (where the spectral library lacks compositions between Fo_{68} and Fo_{90} that would likely provide an even better fit to ALH A77005). Nonetheless, the derived $Fo_{\#}$ is within 4–9 of known compositions. Relative to Model 1, Model 2 exhibits a significant degradation in the fit across the entire spectrum (Fig. 18**b**), and the modeled mineralogy bears this out, with a significant overestimation of the feldspar content and underestimation of the olivine content, although pyroxene is within the range of measured values. The uncertainties on these abundances are higher by up to a factor of three relative to Model 1. The derived solid solution composition of olivine is even lower than in Model 1 (Fo_{59}), suggesting that limiting the olivines represented in the library to only Fo_{91} and Fo_{0} is having a significant effect on the quality of the fit to this lithology rich in intermediate olivine.

Chassigny is a dunite comprised of >90 vol% olivine with ≤ 5 vol% each pyroxene and feldspar. Model 1 produces an excellent fit to the measured spectrum, matching the band positions and amplitudes well (Fig. 18**a**). The modeled abundance of olivine (93 vol%) is within 1 vol% of the known value (92 vol%), and the composition is estimated at Fo_{69}, which is also within 1 mol% of the known value (Fo_{68}). In Model 2, however, there is a significant misfit between the measured and modeled spectra (Fig. 18**b**), with both band positions and amplitudes being poorly matched. The abundance of olivine in the meteorite is underestimated by almost 25 vol%, with the majority of the difference going into a significant overestimate of the abundance of plagioclase. The composition of the olivine is only underestimated by 8 mol%, however, suggesting that the strength and narrowness of the olivine features that dominate the measured spectrum limit how far the modeled composition can stray from the actual composition, instead resulting in the increase of a phase with weaker and broader features (feldspar).

In summary, all five meteorites contain olivine, and olivine is identified from all five meteorites' spectra in both models (10 total models/cases). In cases where a compositional suite of olivine spectra is available to make the best fit (Model 1), modeled olivine abundances are within the range of measured abundances in four out of five cases, and within 5% of the measured abundance (which is within the uncertainty) in the fifth case. In these cases, the mol% forsterite is modeled within the range of measured values in three cases, and is within 10 $Fo_{\#}$ in the other two cases. These results suggest that for olivine-bearing lithologies libraries with spectra representing a range of olivine compositions (Model 1) generally are capable of accurately identifying the abundance of olivine to within 5 vol% and the $Fo_{\#}$ within 10. I note that this is a conservative estimate that does not take into account misfits derived from minor inaccuracies in the modeling of other phases, such as plagioclase and pigeonite, which also have some effect on the derived abundances and compositions of olivine—improvements to the fits to other phases likely will improve the results for olivine.

In models where only two olivine compositions (forsterite and fayalite) are available in the spectral library (Model 2), underestimates of olivine abundance up to 24 vol% result for meteorites with the greatest amount of measured olivine (ALH A77005 and Chassigny). In model 2 cases, $Fo_{\#}$ is modeled within the range of measured values in only one case (EET A79001); it is within or near 10 mol% in two cases (ALH A77005 and Chassigny), and is underestimated by up to 35 mol% in two cases (Nakhla and Lafayette). In the cases of Nakhla and Lafayette, the model nevertheless did use the fayalitic olivine to match iron-rich olivines in the meteorites. Spectral libraries containing only near-end member olivine solid solution compositions (Model 2) may significantly underestimate the true abundance of olivine if olivine is a major component of the lithology, and derived solid solution compositions likely could only be conservatively interpreted as identifying olivine as iron- or magnesium rich.

As mentioned above, in the two meteorites having olivine as the dominant phase, ALH A77005 and Chassigny, there is a significant difference between the results derived from a spectral library representing a broad range of olivine compositions (Model 1) and one that has only (near-) end member compositions (Model 2). If intermediate compositions in the meteorites are not represented in the spectral library, the spectral fits are obviously degraded and the derived abundances of olivine are underestimated by up to 25%, although solid solution compositions are within ~10% in the two cases examined here. The features of olivine are so strong in these meteorites' spectra that the best fits for Model 2 are achieved by using greater abundances of relatively spectrally bland phases (feldspars) rather than by using appropriate abundances of olivine, but which have band positions that are shifted farther away from the features in the meteorite spectra or that do not resemble an olivine spectrum when mixed linearly. This occurs because olivine features shift in wavenumber as a function of cation substitution. Therefore, a linear mixture of olivine spectra representing (near-) end member compositions (e.g., Fo_{90} and Fo_{10}) cannot reproduce the spectrum of an intermediate composition olivine (e.g., Fo_{54}) because the spectral features of the mixture do not reproduce the shifts in band position, resulting in additional minima in the mixture spectrum, and the net result that the mixture spectrum does not resemble that of intermediate olivine (Fig. 19). At low abundances, this difference does not have as strong an effect on the modeled spectrum of the whole rock, but it has a very strong effect in cases where olivine abundance is high. In cases where olivine abundance is not known a priori, all olivine-bearing lithologies will be most reliably modeled by libraries that contain spectra representing a range of olivine compositions.

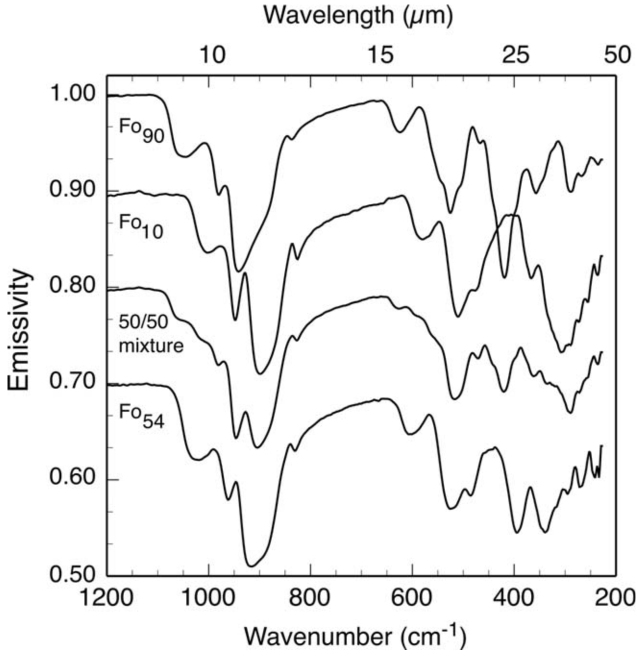

Fig. 19. Demonstration that a linear mixture of olivine spectra representing near-end member compositions (Fo_{90} and Fo_{10}) does not match the spectrum of an intermediate composition. Spectra are offset for clarity.

6. Summary

In the study of planetary surfaces, the presence of olivine is an indicator of a low-silica environment and high temperature crystallization. Solid solution compositions, if they can be determined, are indicative of the chemistry of their parent magmas and the evolution of those magmas through processes of melting, re-equilibration, and differentiation. The literature describing the transmittance spectra of Mg–Fe olivines shows that these data can be used to determine the relative proportions of the Mg and Fe cations with substantial accuracy using determinative curves based on band position. In general, band positions move to lower wavenumbers (longer wavelengths) across the forsterite–fayalite compositional binary in a strongly linear manner. Specific feature shifts in some transmittance data have been described by fits containing a slight break in slope near Fo_{70}, which may be accompanied by a small offset as well; both traits are attributed to structural changes in olivine brought about by distortion of the crystal lattice around Fe in the octahedral site. Unlike transmittance spectra, laboratory reflectance and emissivity spectra are directly comparable to TIR remote sensing data (measured as emission). Because they are sensitive to both the real and imaginary indices of refraction, reflectance and emissivity spectra of olivines in the Mg–Fe series display band shapes and positional shifts that are very similar to, but do not match exactly, the variations observed in transmittance data. Nonetheless, olivine composition can be determined from band positions in reflectance and emissivity spectra, as well as from the relative strengths of some bands, and the positions of the primary and secondary Christiansen features. Although most features can be correlated between transmittance and reflectance/emissivity spectra, the latter measurements do exhibit an additional absorption in the 550–500 cm^{-1} region that is not observed in transmittance spectra; this feature also follows a linear trend in position as a function of composition. New linear least squares models of the emissivity spectra of olivine-bearing Martian meteorites enable a preliminary estimation of the accuracy with which olivine abundance and solid solution composition can be derived from the spectra of mixtures, and demonstrate that a range of olivine compositions is needed to obtain the most accurate results.

Based on their diagnostic thermal infrared spectral features, olivines have been identified in a wide array of thermal infrared

Please cite this article as: Hamilton, V.E., (2010), doi:10.1016/j.chemer.2009.12.005

spectra of planetary materials and have been interpreted as being present on the surfaces of Mercury, the Moon, Mars, and a number of asteroids. The precision with which the compositions on planetary surfaces can be constrained from band position data will be related to the spectral resolution and signal-to-noise of the data, as well as the presence of other phases, which add linearly in the measured spectrum, and these factors should be considered in analyzing remote sensing data. The most compelling analyses of remotely sensed surfaces proposed to contain olivine will either demonstrate complete spectral shapes consistent with olivine or will identify the majority of the major spectral features described here, with the positions of these features being consistent with a single composition or a continuous range of compositions along the Mg–Fe binary.

Acknowledgements

I would like to thank S.A. Morse (U. Mass.) for providing the majority of olivine samples used to measure the emissivity data presented here and for acquiring and providing the microprobe analysis of sample KI3372. Will Koeppen (U. Hawaii) undertook the challenging task of isolating several of the Kiglapait olivine samples from the mafic concentrates in which they were provided; he also acquired many of the olivine emissivity spectra used for the new analyses presented in this manuscript. I would also like to thank Karen Stockstill (U. Hawaii) for performing electron microprobe analyses of several olivine samples that ultimately did not appear in this manuscript. I am grateful to Klaus Keil for the invitation to write this review, and appreciate his patience during its preparation. Will Koeppen and an anonymous reviewer offered valuable comments that have improved the final manuscript; any lingering errors or omissions are mine alone. I would like to recognize the generosity of the scientists who made their published spectral data available online; many of the new analyses presented here would not have been possible or would have been much more difficult to conduct without ready access to these data. Portions of this work were supported by NASA's Planetary Geology and Geophysics Program (NNX08BB10G).

References

Bandfield, J.L., 2002. Global mineral distributions on Mars. J. Geophys. Res., 107, doi:10.1029/2001JE001510.

Bandfield, J.L., Hamilton, V.E., Christensen, P.R., 2000. A global view of Martian surface compositions from MGS-TES. Science 287, 1626–1630.

Barucci, M.A., Fornasier, S., Dotto, E., Lamy, P.L., Jorda, L., Groussin, O., Brucato, J.R., Carvano, J., Alvarez-Candal, A., Cruikshank, D., Fulchignoni, M., 2008. Asteroids 2867 Steins and 21 Lutetia: surface composition from far infrared observations with the Spitzer Space Telescope. Astron. Astrophys. 477, 665–670.

Barucci, M.A., Dotto, E., Brucato, J.R., Müller, T.G., Morris, P., Doressoundiram, A., Fulchignoni, M., De Sanctis, M.C., Owen, T., Crovisier, J., Le Bras, A., Colangeli, L., Mennella, V., 2002. 10 Hygiea: ISO infrared observations. Icarus 156, 202–210.

Berkley, J.L., Keil, K., and Prinz, M., 1980. Comparative petrology and origin of Governador Valadares and other nakhlites. Proceedings of the 11th Lunar Planetary Science Conference, pp. 1089–1102.

Bowey, J.E., Lee, C., Tucker, C., Hofmeister, A.M., Ade, P.A.R., Barlow, M.J., 2001. Temperature effects on the 15–85 μm spectra of olivines and pyroxenes. Mon. Not. R. Astron. Soc. 325, 886–896.

Bradley, J.P., 2004. Interplanetary dust particles. In: Holland, H.D., Turekian, K.K. (Eds.), Treatise on Geochemistry. Elsevier, Oxford, pp. 1.

Burns, R.G., Huggins, F.E., 1972. Cation determinative curves for Mg–Fe–Mn olivines from vibrational spectra. Am. Miner. 57, 967–985.

Carvano, J.M., Migliorini, A., Barucci, A., Segura, M., the CIRS Team, 2007. Constraining the surface properties of Saturn's icy moons, using Cassini/CIRS emissivity spectra. Icarus 187, 574–583.

Chase Jr., S.C., Miner, E.D., Morrison, D., Munch, G., Neugebauer, G., 1976. Mariner 10 infrared radiometer results: temperatures and thermal properties of the surface of Mercury. Icarus 28, 565–578.

Chihara, H., Koike, C., Tsuchiyama, A., 2001. Low-temperature optical properties of silicate particles in the far-infrared region. Publ. Astron. Soc. Jpn. 53, 243–250.

Christensen, P.R., 1982. Martian dust mantling and surface composition: interpretation of thermophysical properties. J. Geophys. Res. 87, 9985–9998.

Christensen, P.R., Moore, H.J., 1992. The martian surface layer. In: Kieffer, H.H., Jakosky, B.M., Snyder, C.W., Matthews, M.S. (Eds.), Mars. University of Arizona Press, Tucson, AZ, pp. 686–729.

Christensen, P.R., Bandfield, J.L., Smith, M.D., Hamilton, V.E., Clark, R.N., 2000a. Identification of a basaltic component on the Martian surface from Thermal Emission Spectrometer data. J. Geophys. Res. 105, 9609–9621.

Christensen, P.R., Bandfield, J.L., Hamilton, V.E., Howard, D.A., Lane, M.D., Piatek, J.L., Ruff, S.W., Stefanov, W.L., 2000b. A Thermal Emission Spectral library of rock-forming minerals. J. Geophys. Res. 105, 9735–9739.

Christensen, P.R., Bandfield, J.L., Clark, R.N., Edgett, K.S., Hamilton, V.E., Hoefen, T., Kieffer, H.H., Kuzmin, R.O., Lane, M.D., Malin, M.C., Morris, R.V., Pearl, J.C., Pearson, R., Roush, T.L., Ruff, S.W., Smith, M.D., 2000c. Detection of crystalline hematite mineralization on Mars by the Thermal Emission Spectrometer: evidence for near-surface water. J. Geophys. Res. 105, 9623–9642.

Christensen, P.R., Bandfield, J.L., Hamilton, V.E., Ruff, S.W., Kieffer, H.H., Titus, T.N., Malin, M.C., Morris, R.V., Lane, M.D., Clark, R.N., Jakosky, B.M., Mellon, M.T., Pearl, J.C., Conrath, B.J., Smith, M.D., Clancy, R.T., Kuzmin, R.O., Roush, T.L., Mehall, G.L., Gorelick, N., Bender, K., Murray, K., Dason, S., Greene, E., Silverman, S., Greenfield, M., 2001. Mars Global Surveyor Thermal Emission Spectrometer experiment: investigation description and surface science results. J. Geophys. Res. 106, 23,823–23,871.

Christensen, P.R., Wyatt, M.B., Glotch, T.D., Rogers, A.D., Anwar, S., Arvidson, R.E., Bandfield, J.L., Blaney, D.L., Budney, C., Calvin, W.M., Fallacaro, A., Fergason, R.L., Gorelick, N., Graff, T.G., Hamilton, V.E., Hayes, A.G., Johnson, J.R., Knudson, A.T., McSween Jr., H.Y., Mehall, G.L., Mehall, L.K., Moersch, J.E., Morris, R.V., Smith, M.D., Squyres, S.W., Ruff, S.W., Wolff, M.J., 2004a. Mineralogy at Meridiani Planum from the Mini-TES experiment on the Opportunity rover. Science 306, 1733–1739.

Christensen, P.R., Ruff, S.W., Fergason, R.L., Knudson, A.T., Anwar, S., Arvidson, R.E., Bandfield, J.L., Blaney, D.L., Budney, C., Calvin, W.M., Glotch, T.D., Golombek, M.P., Gorelick, N., Graff, T.G., Hamilton, V.E., Hayes, A., Johnson, J.R., McSween Jr., H.Y., Mehall, G.L., Mehall, L.K., Moersch, J.E., Morris, R.V., Rogers, A.D., Smith, M.D., Squyres, S.W., Wolff, M.J., Wyatt, M.B., 2004b. Initial results from the Mini-TES experiment in Gusev crater from the Spirit rover. Science 305, 837–842.

Clark, R.N., Swayze, G.A., Wise, R.A., Livo, K.E., Hoefen, T.M., Kokaly, R.F., and Sutley, S.J., 2007. USGS digital spectral library splib06a. US Geological Survey, Digital Data Series 231, http://speclab.cr.usgs.gov/spectral.lib06.

Cohen, M., Witteborn, F.C., Roush, T., Bregman, J., Wooden, D., 1998. Spectral irradiance calibration in the infrared. VIII. 5–14 micron spectroscopy of the asteroids Ceres, Vesta, and Pallas. Astronom. J. 115, 1671–1679.

Conel, J.E., 1969. Infrared emissivities of silicates: experimental results and a cloudy atmosphere model of spectral emission from condensed particulate mediums. J. Geophys. Res. 74, 1614–1634.

Day, K.L., 1976. Temperature dependence of mid-infrared silicate absorption. Ap. J. 203, L99–L101.

Deer, W.A., Howie, R.A., Zussman, J., 1992. In: An Introduction to the Rock-Forming Minerals. Longman, Essex.

Devarajan, V., Funck, E., 1975. Normal coordinate analysis of the optically active vibrations (k=0) of crystalline magnesium orthosilicate Mg_2SiO_3 (forsterite). J. Chem. Phys. 62, 3406–3411.

Donahue, T.M., Russell, C.T., 1997. The Venus atmosphere and ionosphere and their interaction with the solar wind: an overview. In: Bougher, S.W., Hunten, D.M., Phillips, R.J. (Eds.), Venus II: Geology, Geophysics, Atmosphere, and Solar Wind Environment. University of Arizona Press, Tucson, pp. 3–31.

Dotto, E., Barucci, M.A., Brucato, J.R., Müller, T.G., Carvano, J., 2004. 308 Polyxo: ISO-SWS spectrum up to 26 micron. Astron. Astrophys. 427, 1081–1084.

Dotto, E., Barucci, M.A., Müller, T.G., Brucato, J.R., Fulchignoni, M., Mennella, V., Colangeli, L., 2002. ISO observations of low and moderate albedo asteroids. Astron. Astrophys. 393, 1065–1072.

Dotto, E., Mueller, T.G., Barucci, M.A., Encrenaz, T., Knacke, R.F., Lellouch, E., Doressoundiram, A., Crovisier, J., Brucato, J.R., Colangeli, L., Mennella, V., 2000. ISO results on bright Main Belt asteroids: PHT-S observations. Astron. Astrophys. 358, 1133–1141.

Duke, D.A., Stephens, J.D., 1964. Infrared investigation of the olivine group minerals. Am. Miner. 49, 1388–1406.

Dunn, T.L., McSween Jr., H.Y., Christensen, P.R., 2007. Thermal emission spectra of terrestrial alkaline volcanic rocks: applications to Martian remote sensing. J. Geophys. Res., 112, doi:10.1029/2006JE002766.

Edwards, C.S., Christensen, P.R., Hamilton, V.E., 2008. Evidence for extensive olivine-rich basalt bedrock outcrops in Ganges and Eos chasmas, Mars. J. Geophys. Res., 113, doi:10.1029/2008JE003091.

Emery, J.P., Cruikshank, D., Van Cleve, J., 2006. Thermal emission spectroscopy (5.2–38 μm) of three Trojan asteroids with the Spitzer Space Telescope: detection of fine-grained silicates. Icarus 182, 496–512.

Emery, J.P., Sprague, A.L., Witteborn, F.E., Colwell, J.E., Kozlowski, R.W.H., Wooden, D.H., 1998. Mercury: thermal modeling and mid-infared (5–12 μm) observations. Icarus 136, 104–123.

Estep, P.A., Kovach, J.J., Karr Jr., C., 1971. Infrared vibrational spectroscopic studies of minerals from Apollo 11 and Apollo 12 lunar samples. Proc. Sec. Lunar Sci. Conf. 3, 2137–2151.

Please cite this article as: Hamilton, V.E., (2010), doi:10.1016/j.chemer.2009.12.005

Estep, P.A., Kovach, J.J., Waldstein, P., Karr Jr., C., 1972. Infrared and Raman spectroscopic studies of structural variations in minerals from Apollo 11, 12, 14, and 15 samples. Geochim. Cosmochim. Acta 3, 3047–3067.

Fabian, D., Henning, T., Jäger, C., Mutschke, H., Dorschner, J., Wehrhan, O., 2001. Steps toward interstellar silicate mineralogy: VI. Dependence of crystalline olivine IR spectra on iron content and particle shape. Astron. Astrophys. 378, 228–238.

Feely, K.C., Christensen, P.R., 1999. Quantitative compositional analysis using Thermal Emission Spectroscopy: application to igneous and metamorphic rocks. J. Geophys. Res. 104, 24195–24210.

Fegley Jr., B., Klingelhöfer, G., Lodders, K., Widemann, T., 1997. Geochemistry of surface–atmosphere interactions on Venus. In: Bougher, S.W., Hunten, D.M., Phillips, R.J. (Eds.), Venus II: Geology, Geophysics, Atmosphere, and Solar Wind Environment. University of Arizona Press, Tucson, pp. 591–636.

Fischer, E.M., 1995. Quantitative Compositional Analysis of the Lunar Surface from Reflectance Spectroscopy: Iron, Aluminum and a Model for Removing the Optical Effects of Space Weathering. Ph.D. Thesis, Brown University.

Gehrz, R.D., Reach, W.T., Woddward, C.E., Kelley, M.S., 2006. Infrared observations of comets with the Spitzer Space Telescope. Adv. Space Res. 38, 2031–3028.

Glotch, T.D., Bandfield, J.L., 2006. Determination and interpretation of surface and atmospheric Miniature Thermal Emission Spectrometer spectral end-members at the Meridiani Planum landing site. J. Geophys. Res., 111, doi:10.1029/2005JE002671.

Goetz, A.F.H., 1968. Differential infrared lunar emission spectroscopy. J. Geophys. Res. 73, 1455–1466.

Goodrich, C.A., 1992. Ureilites: a critical review. Meteoritics 27, 327–352.

Hamilton, V.E., 2000. Thermal infrared emission spectroscopy of the pyroxene mineral series. J. Geophys. Res. 105, 9701–9716.

Hamilton, V.E., Christensen, P.R., 2000. Determining the modal mineralogy of mafic and ultramafic igneous rocks using Thermal Emission Spectroscopy. J. Geophys. Res. 105, 9717–9733.

Hamilton, V.E., Lucey, P.G., 2005. One spectrometer, two spectra: complementary hemispherical reflectance and Thermal Emission Spectroscopy using a single FTIR instrument. Lunar Planet. Sci. XXXVI Abstract #1272.

Hamilton, V.E., Christensen, P.R., 2005. Evidence for extensive, olivine-rich bedrock on Mars. Geology 33, 433–436 doi:410.1130/.21251.

Hamilton, V.E., Christensen, P.R., McSween Jr., H.Y., 1997. Determination of Martian meteorite lithologies and mineralogies using vibrational spectroscopy. J. Geophys. Res. 102, 25,593–525,603.

Hamilton, V.E., Christensen, P.R., McSween Jr., H.Y., Bandfield, J.L., 2003. Searching for the source regions of Martian meteorites using MGS TES: integrating Martian meteorites into the global distribution of volcanic materials on Mars. Meteor. Planet. Sci. 38, 871–885.

Hapke, B., 1981. Bidirectional reflectance spectroscopy I. Theory. J. Geophys. Res. 86, 3039–3054.

Hapke, B., 1993. In: Theory of Reflectance and Emittance Spectroscopy. Cambridge University Press, New York.

Hapke, B., van Horn, H., 1963. Photometric studies of complex surfaces, with applications to the Moon. J. Geophys. Res. 68, 4545–4570.

Head, J.W., Murchie, S.L., Prockter, L.M., Robinson, M.S., Solomon, S.C., Strom, R.G., Chapman, C.R., Watters, T.R., McClintock, W.E., Blewett, D.T., Gillis-Davis, J.J., the MESSENGER Team, 2008. Volcanism on Mercury: evidence from the first MESSENGER flyby. Science 321, 69–71.

Helbert, J., Jessberger, E., Benkhoff, J., Arnold, G., Banaszkiewicz, M., Bischoff, A., Blecka, M., Calcutt, S., Colangeli, L., Coradini, A., Erard, S., Fonti, S., Killen, R., Knollenberg, J., Kührt, E., Mann, I., Mall, U., Moroz, L., Peter, G., Rataj, M., Robinson, M.S., Spohn, T., Sprague, A., Stöffler, D., Taylor, F., Warrell, J., 2005. MERTIS—a thermal infrared imaging spectrometer for the Bepi-Columbo mission. Lunar Planet. Sci. XXXVI Abstract no. 1753.

Henderson, B.G., Jakosky, B.M., 1994. Near-surface thermal gradients and their effects on mid-infrared emission spectra of planetary surfaces. J. Geophys. Res. 99, 19063–19073.

Henderson, B.G., Jakosky, B.M., 1997. Near-surface thermal gradients and mid-IR emission spectra: a new model including scattering and application to real data. J. Geophys. Res. 102, 6567–6580.

Henning, T., Mutschke, H., 1997. Low-temperature infrared properties of cosmic dust analogues. Astron. Astrophys. 327, 743–754.

Heras, A.M., Morris, P.W., Vandenbussche, B., and Müller, T.G., 2000, Asteroid 4 Vesta as seen with the ISO Short Wavelength Spectrometer: Thermal Emission Spectroscopy and analysis of dust, disks, and regoliths, pp. 205–212.

Hoefen, T.M., Clark, R.N., Bandfield, J.L., Smith, M.D., Pearl, J.C., Christensen, P.R., 2003. Discovery of olivine in the Nili Fossae region of Mars. Science 302, 627–630.

Hofmeister, A.M., 1987. Single-crystal absorption and reflection infrared spectroscopy of forsterite and fayalite. Phys. Chem. Miner. 14, 499–513.

Hofmeister, A.M., 1997. Infrared reflectance spectra of fayalite, and absorption data from assorted olivines, including pressure and isotope effects. Phys. Chem. Min. 24, 535–546.

Hofmeister, A.M., Pitman, K.M., 2007. Evidence for kinks in structural and thermodynamic properties across the forsterite–fayalite binary from thin-film IR absorption spectra. Phys. Chem. Miner. 34, 319–333.

Hunt, G.R., Logan, L.M., 1972. Variation of single particle mid-infrared emission spectrum with particle size. Appl. Opt. 11, 142–147.

Iishi, K., 1978. Lattice dynamics of forsterite. Am. Miner. 63, 1198–1208.

Jäger, C., Molster, F.J., Dorschner, J., Henning, T., Mutschke, H., Waters, L.B.F.M., 1998. Steps toward interstellar silicate mineralogy: IV. The crystalline revolution. Astron. Astrophys. 339, 904–916.

Johnson, J.R., 2002. Thermal infrared spectroscopy of experimentally shocked anorthosite and pyroxenite: implications for remote sensing of Mars. J. Geophys. Res., 107, doi:10.1029/2001JE001517.

Keller, L.P., 32 coworkers, 2006. Infrared spectroscopy of comet 81P/Wild 2 samples returned by Stardust. Science 314, 1728–1731.

Koeppen, W.C., Hamilton, V.E., 2008. The global distribution, composition, and abundance of olivine on the surface of Mars from thermal infrared data. J. Geophys. Res., 113, doi:10.1029/2007JE002984.

Koike, C., Chihara, H., Tsuchiyama, A., Suto, H., Sogawa, H., Okuda, H., 2003. Compositional dependence of infrared absorption spectra of crystalline silicate: II. Natural and synthetic olivines. Astron. Astrophys. 399, 1101–1107.

Lane, M.D., 2007. Mid-infrared emission spectroscopy of sulfate and sulfate-bearing minerals. Am. Miner. 92, 1–18, doi:10.2138/am.2007.2170.

Lehmann, H., Dutz, H., Koltermann, M., 1961. Ultrarotspektroskopische Untersuchungen zur Mischkristallreihe Forsterit–Fayalit. Ber. Deutsche Keram. Ges. 38, 512–514.

Lim, L.F., McConnochie, T.H., Bell, J.F.I., Hayward, T.L., 2005. Thermal infrared (8–13 μm) spectra of 29 asteroids: the Cornell mid-infrared asteroid spectroscopy (MIDAS) survey. Icarus 173, 385–408.

Lisse, C.M., Van Cleve, J., Adams, A.C., A'Hearn, M.F., Fernandez, Y.R., Farnham, T.L., Armus, L., Grillmair, C.J., Ingalls, J., Belton, M.J.S., Groussin, o, McFadden, L.A., Meech, K.H., Schultz, P.H., Clark, B.C., Feaga, L.M., Sunshine, J.M., 2006. Spitzer spectral observations of the Deep Impact ejecta. Science 313, 635–640.

Logan, L.M., Hunt, G.R., 1970. Emission spectra of particulate silicates under simulated lunar conditions. J. Geophys. Res. 75, 6539–6548.

Lyon, R.J.P., 1962. Minerals in the Infrared: A Critical Bibliography. Stanford Research Institute, Menlo Park, California.

Lyon, R.J.P., Tuddenham, W.M., Thompson, C.S., 1959. Quantitative mineralogy in 30 minutes. Econ. Geol. 54, 1047–1055.

Mason, B., 1981. ALH A77005 petrographic description. Antarct. Meteor. Newslett. 4, 12.

Maturilli, A., Helbert, J., Moroz, L., 2008. The Berlin emissivity database (BED). Planet. Space Sci. 56, 420–425.

McSween Jr., H.Y., Taylor, L.A., Stolper, E.M., 1979. Allan Hills 77005: a new meteorite type found in Antarctica. Science 204, 1201–1203.

McSween Jr., H.Y., Wyatt, M.B., Gellert, R., Bell III, J.F., Morris, R.V., Herkenhoff, K.E., Crumpler, L.S., Milam, K.A., Stockstill, K.R., Tornabene, L.L., Arvidson, R.E., Bartlett, P., Blaney, D.L., Cabrol, N.A., Christensen, P.R., Clark, B.C., Crisp, J.A., Des Marais, D.J., Economou, T., Farmer, J.D., Farrand, W.H., Ghosh, A., Golombek, M.P., Gorevan, S., Greeley, R., Hamilton, V.E., Johnson, J.R., Joliff, B.L., Klingelhöfer, G., Knudson, A.T., McLennan, S.M., Ming, D.W., Moersch, J.E., Rieder, R., Ruff, S.W., Schroder, C., de Souza Jr., P.A., Squyres, S.W., Wanke, H., Wang, A., Yen, A.S., Zipfel, J., 2006. Characterization and petrologic interpretation of olivine-rich basalts at Gusev Crater, Mars. J. Geophys. Res., 111, doi:10.1029/2005JE002477.

Mellon, M.T., Jakosky, B.M., Kieffer, H.H., Christensen, P.R., 2000. High resolution thermal inertia mapping from the Mars Global Surveyor Thermal Emission Spectrometer. Icarus 148, 437–455.

Mennella, V., Brucato, J.R., Colangeli, L., Palumbo, P., Rotundi, A., Bussoletti, E., 1998. Temperature dependence of the absorption coefficient of cosmic analog grains in the wavelength range 20 microns to 2 millimeters. Ap. J. 496, 1058–1066.

Meyer, C., 2003. Mars Meteorite Compendium (JSC #27672 Rev. C), http://www-curator.jsc.nasa.gov/curator/antmet/mmc/mmc.htm: Houston, TX, Office of the Curator, NASA-JSC.

Michalski, J.R., Kraft, J.D., Diedrich, T., Sharp, T.G., Christensen, P.R., 2003. Thermal emission spectroscopy of the silica polymorphs and considerations for remote sensing of Mars. Geophys. Res. Lett., 30, doi:10.1029/2003GL018354.

Michalski, J.R., Kraft, M.D., Sharp, T.G., Williams, L.B., Christensen, P.R., 2006. Emission spectroscopy of clay minerals and evidence for poorly crystalline aluminosilicates on Mars from Thermal Emission Spectrometer data. J. Geophys. Res., 11, doi:10.1029/2005JE002438.

Milam, K.A., McSween Jr., H.Y., Christensen, P.R., 2007. Plagioclase compositions derived from Thermal Emission Spectra of compositionally complex mixtures: Implications for Martian feldspar mineralogy. J. Geophys. Res., 112, doi:10.1029/2006JE002880.

Mills, F.P., Brown, M.E., 2000. Thermal infrared spectroscopy of Europa and Callisto. J. Geophys. Res. 105, 15,051–015,059.

Miyamoto, M., 1986. Diffuse reflectance from 0.25 to 25 μm of the Yamato-691 enstatite chondrite. Memoirs of the National Institute of Polar Research 46, 123–130.

Miyamoto, M., 1987. Infrared diffuse reflectances (2.5–25 μm) of some meteorites. Icarus 70, 146–152.

Miyamoto, M., Zolensky, M.E., 1994. Infrared diffuse reflectance spectra of carbonaceous chondrites: amount of hydrous materials. Meteoritics 29, 849–853.

Moersch, J.E., Christensen, P.R., 1991. Modeling particle size effects on the emissivity spectra of minerals in the thermal infrared. Bull. Am. Astron. Soc. 23, 1183.

Morlok, A.K., öhler, M., Bowey, J.E., Grady, M.M., 2006a. FT-IR microspectroscopy of extraterrestrial dust grains: comparison of measurement techniques. Planet. Space Sci. 54, 599–611.

Morlok, A., Bowey, J., Köhler, M., Grady, M.M., 2006b. FTIR 2–16 micron spectroscopy of micron-sized olivines from primitive meteorites. Met. Planet. Sci. 41, 773–784.

Morse, S.A., 1996. Kiglapait mineralogy III: olivine compositions and Rayleigh fractionation models. J. Pet. 37, 1037–1061.

Murchie, S.L., Watters, T.R., Robinson, M.S., Head, J.W., Strom, R.G., Chapman, C.R., Solomon, S.C., McClintock, W.E., Prockter, L.M., Domingue, D.L., Blewett, D.T., the MESSENGER Team, 2008. Geology of the Caloris Basin, Mercury: a new view from MESSENGER. Science 321, 73–76.

Murcray, F.H., Murcray, D.J., Williams, W.J., 1970. Infrared emissivity of lunar surface features: I. Balloon-borne observations. J. Geophys. Res. 74, 2662–2669.

Mustard, J.F., Hays, J.E., 1997. Effects of hyperfine particles on reflectance spectra from 0.3 to 25 μm. Icarus 125, 145–163.

Mustard, J.F., Poulet, F., Head, J.W., Mangold, N., Bibring, J.-P., Pelkey, S.M., Fasset, C.I., Langevin, Y., Neukum, G., 2007. Mineralogy of the Nili Fossae region with OMEGA/MEx data: 1) Ancient impact melt in the Isidis Basin and implications for the transition from the Noachian to Hesperian. J. Geophys. Res., 112, doi:10.1029/2006JE002834.

Nash, D.B., Salisbury, J.W., Conel, J.E., Lucey, P.G., Christensen, P.R., 1993. Evaluation of infrared emission spectroscopy for mapping the Moon's composition from lunar orbit. J. Geophys. Res. 98, 23,535–23,552.

Nicodemus, F.E., 1965. Directional reflectance and emissivity of an opaque surface. Appl. Opt. 4, 767–773.

Oehler, O., Günthard, H.H., 1969. Low-temperature infrared spectra between 1200 and 20 cm^{-1} and normal-coordinate analysis of silicates with olivine structure. J. Chem. Phys. 51, 4719–4728.

Omori, K., 1967. Infrared study of mechanical mixtures of quartz, orthoclase, and oligoclase from 11 to 25 microns. Miner. J. 5, 169–179.

Osawa, T., Kagi, H., Nagao, K., 2001. Mid-infrared transmission spectra of individual Antarctic micrometeorites and carbonaceous chondrites. Antarct. Meteor. Res. 14, 71–80.

Paige, D.A., Foote, M.C., Greenhagen, B.T., Schofield, J.T., Calcutt, S., Vasavada, A.R., Preston, D.J., Taylor, F.W., Allen, C.C., Snook, K.J., Jakosky, B.M., Murray, B.C., Soderblom, L.A., Jau, B., Loring, S., Bulharowski, J., Bowles, N.E., Thomas, I.R., Sullivan, M.T., Avis, C., DeJong, E.M., Hartford, W., and McCleese, D.J., 2009. The Lunar Reconnaissance Orbiter Diviner lunar radiometer experiment. Space Sci. Rev., 10.1007/s1121400995292.

Piatek, J.L., 1997. Vibrational Spectroscopy of Clay Minerals: Implications for Remote Sensing of Terrestrial Planetoids. M.S. Thesis, Arizona State University, 78pp.

Pieters, C.M., Fischer, E.M., Rode, O., Basu, A., 1993. Optical effects of space weathering: the role of the finest fraction. J. Geophys. Res. 98, 20,817–820,824.

Pieters, C.M., Klima, R.L., Hiroi, T., Dyar, M.D., Lane, M.D., Treiman, A.H., Noble, S.K., Sunshine, J.M., Bishop, J.L., 2008. Martian dunite NWA 2737: integrated spectroscopic analyses of brown olivine. J. Geophys. Res., 113, doi:10.1029/2007JE002939.

Presley, M.A., Christensen, P.R., 1997. Thermal conductivity measurements of particulate materials. Part II: Results. J. Geophys. Res. 102, 6566–6651.

Price, S.D., 2002. Infrared observations of asteroids from space: the past and future. Meteor. Planet. Sci. 37, 1909–1917.

Prinz, M., Hlava, P.H., Keil, K., 1974. The Chassigny meteorite: a relatively iron-rich cumulate dunite. Meteoritics 9, 393–394.

Putzig, N.E., Mellon, M.T., Kretke, K.A., Arvidson, R.E., 2005. Global thermal inertia and surface properties of Mars from the MGS mapping mission. Icarus 173, 325–341.

Ramsey, M.S., Christensen, P.R., 1998. Mineral abundance determination: quantitative deconvolution of Thermal Emission Spectra. J. Geophys. Res. 103, 577–596.

Raynal, P.I., Quirico, E., Borg, J., Deboffle, D., Dumas, P., d'Hendecort, L., Bibring, J.-P., Langevin, Y., 2000. Synchrotron infrared microscopy of micron-sized extraterrestrial grains. Planet. Space Sci. 48, 1329–1339.

Reynard, B., 1991. Single-crystal infrared reflectivity of pure Mg_2SiO_4 forsterite and $(Mg_{0.86},Fe_{0.14})_2SiO_4$ olivine: new data and a reappraisal. Phys. Chem. Miner. 18, 19–25.

Rogers, A.D., Aharonson, O., 2008. Mineralogical composition of sands in Meridiani Planum determined from Mars Exploration Rover data and comparison to orbital measurements. J. Geophys. Res., 113, doi:10.1029/2007JE002995.

Rogers, A.D., Christensen, P.R., Bandfield, J.L., 2005. Compositional heterogeneity of the ancient Martian crust: surface analysis of Ares Vallis bedrock with THEMIS and TES data. J. Geophys. Res., 110, doi:10.1029/2005JE002399.

Ruff, S.W., 1998. Quantitative Thermal Infrared Emission Spectroscopy Applied to Granitoid Petrology. Ph.D. Thesis, Arizona State University, 234 p.

Ruff, S.W., 2004. Spectral evidence for zeolite in the dust on Mars. Icarus 168, 131–143.

Ruff, S.W., Christensen, P.R., 2002. Bright and dark regions on Mars: particle size and mineralogical characteristics based on Thermal Emission Spectrometer data. J. Geophys. Res. 107, 5127 doi:5110.1029/2001JE001580.

Ruff, S.W., Christensen, P.R., Barbera, P.W., Anderson, D.L., 1997. Quantitative Thermal Emission Spectroscopy of minerals: a laboratory technique for measurement and calibration. J. Geophys. Res. 102, 14,899–14,913.

Ruff, S.W., Christensen, P.R., Blaney, D.L., Farrand, W.H., Johnson, J.R., Michalski, J.R., Moersch, J.E., Wright, S.P., Squyres, S.W., 2006. The rocks of Gusev Crater as viewed by the Mini-TES instrument. J. Geophys. Res., 111, doi:10.1029/2006JE002747.

Salisbury, J.W., Eastes, J.W., 1985. The effect of particle size and porosity on spectral contrast in the mid-infrared. Icarus 64, 586–588.

Salisbury, J.W., Wald, A., 1992. The role of volume scattering in reducing spectral contrast of reststrahlen bands in spectra of powdered minerals. Icarus 96, 121–128.

Salisbury, J.W., Walter, L.S., and Vergo, N., 1987. Mid-infrared (2.1–25 μm) spectra of minerals: first ed. U.S.G.S., Open File Report, pp. 87–263.

Salisbury, J.W., D'Aria, D.M., Jarosewich, E., 1991a. Midinfrared (2.5–13.5 μm) reflectance spectra of powdered stony meteorites. Icarus 92, 280–297.

Salisbury, J.W., Basu, A., Fischer, E.M., 1997. Thermal infrared spectra of lunar soils. Icarus 130, 125–139.

Salisbury, J.W., Vincent, R.K., Logan, L.M., Hunt, G.R., 1970. Infrared emissivity of lunar surface features, 2, Interpretation. J. Geophys. Res. 75, 2671–2682.

Salisbury, J.W., Walter, L.S., Vergo, N., D'Aria, D.M., 1991b. In: Infrared (2.1–25 μm) Spectra of Minerals. The Johns Hopkins University Press, Baltimore and London.

Salisbury, J.W., Murcray, D.G., Williams, W.J., Blatherwick, R.D., 1995. Thermal infrared spectra of the Moon. Icarus 115, 181–190.

Sandford, S.A., 1984. Infrared transmission spectra from 2.5 to 25 μm of various meteorite classes. Icarus 60, 115–126.

Sandford, S.A., 1993. The mid-infared transmission spectra of Antarctic ureilites. Meteoritics 28, 579–585.

Sandford, S.A., Walker, R.M., 1985. Laboratory infrared transmission spectra of individual interplanetary dust particles from 2.5 to 25 microns. Ap. J. 291, 838–851.

Servoin, J.L., Piriou, B., 1973. Infrared reflectivity and Raman scattering of Mg_2SiO_4 single crystal. Phys. Status Solidi B55, 677–686.

Smith, M.D., Bandfield, J.L., Christensen, P.R., 2000. Separation of atmospheric and surface spectral features in Mars Global Surveyor Thermal Emission Spectrometer (TES) spectra. J. Geophys. Res. 105, 9589–9607.

Sprague, A.L., Witteborn, F., Kozlowski, R., Cruikshank, D., Bartholomew, M., Graps, A., 1992. The Moon: mid-infrared (7.5–11.4 μm) spectroscopy of selected regions. Icarus 100, 73–84.

Sprague, A.L., Emery, J.P., Donaldson, K.L., Russell, R.W., Lynch, D.K., Mazuk, A.L., 2002. Mercury: mid-infrared (3–13.5 μm) observations show heterogeneous composition, presence of intermediate and basic soil types, and pyroxene. Meteor. Planet. Sci. 37, 1255–1268.

Sprague, A.L., Deutsch, L.K., Hora, J., Fazio, G.G., Ludwig, B., Emery, J., Hoffmann, W.F., 2000. Mid-infrared (8.1–12.5 μm) imaging of Mercury. Icarus 147, 421–432.

Sprague, A.L., Donaldson Hanna, K.L., Kozlowski, R.W.H., Helbert, J., Maturilli, A., Warell, J.B., Hora, J.L., 2009. Spectral emissivity measurements of Mercury's surface indicate Mg- and Ca-rich mineralogy, K-spar, Na-rich plagioclase, rutile, with possible perovskite, and garnet. Planet. Space Sci. 57, 364–383.

Staid, M.I., Johnson, J.R., and Gaddis, L.R., 2004. Analysis of Mars Thermal Emission Spectrometer data using large mineral reference libraries. Lunar Planet. Sci. XXXV, Abstract no. 1778, Lunar and Planetary Institute, Houston (CD-ROM).

Stansberry, J.A., Van Cleve, J., Reach, W.T., Cruikshank, D.P., Emery, J.P., Fernandez, Y.R., Meadows, V.S., Su, K.Y.L., Misselt, K., Rieke, G.H., Young, E.T., Werner, M.W., Engelbracht, C.W., Gordon, K.D., Hines, D.C., Kelley, D.M., Morrison, J.E., Muzerolle, J., 2004. Spitzer observations of the dust coma and nucleus of 29P/Schwassmann-Wachmann. Ap. J. S. 154, 463–468.

Suto, H., Koike, C., Sogawa, H., Tsuchiyama, A., Chihara, H., Mizutani, K., 2002. Infrared spectra of fayalite crystal. Astron. Astrophys. 389, 568–571.

Takeda, H., 1991. Comparisons of Antarctic and non-Antarctic achondrites and possible origin of the differences. Geochim. Cosmochim. Acta 55, 35–47.

Tarantino, S.C., Carpenter, M.A., Domeneghetti, M.C., 2003. Strain and local heterogeneity in the forsterite–fayalite solid solution. Phys. Chem. Min. 30, 495–502.

Tarte, P., 1963. Etude infra-rouge des orthosilicates et des orthogermanates—II: Structures du type olivine et monticellite. Spectrochim. Acta 19, 25–47.

Thomson, J.L., Salisbury, J.W., 1993. The mid-infrared reflectance of mineral mixtures (7–14 μm). Rem. Sens. Environ. 45, 1–13.

Tornabene, L.L., Moersch, J.E., McSween Jr., H.Y., Hamilton, V.E., Piatek, J.L., Christensen, P.R., 2008. Surface and crater-exposed lithologic units of the Isidis Basin as mapped by coanalysis of THEMIS and TES derived data products. J. Geophys. Res., 113, doi:10.1029/2007JE002988.

Treiman, A.H., McKay, G.A., Bogard, D.D., Wang, M.-S., Lipschutz, M.E., Mittlefehldt, D.W., Keller, L., Lindstrom, M.M., Garrison, D., 1994. Comparison of the LEW 88516 and ALH A77005 Martian meteorites: similar but distinct. Meteoritics 29, 581–592.

Tyler, A.L., Kozlowski, W.H., Lebofsky, L.A., 1988. Determination of rock type on Mercury and the Moon through remote sensing in the thermal infrared. Geophys. Res. Lett. 15, 808–811.

Vincent, R.K., Hunt, G.R., 1968. Infrared reflectance from mat surfaces. Appl. Opt. 7, 53–59.

Wooden, D.H., Harker, D.E., Woodward, C.E., Butner, H.M., Koike, C., Witteborn, F.C., McMurtry, C.W., 1999. Silicate mineralogy of the dust in the inner coma of Comet C/1995 O1 (Hale-Bopp) pre- and post-perihelion. Astrophys. J. 517, 1034–1058.

Wyatt, M.B., Hamilton, V.E., McSween Jr., H.Y., Christensen, P.R., 2001. Analysis of terrestrial and Martian volcanic compositions using Thermal Emission Spectroscopy: I. Determination of mineralogy, chemistry, and classification strategies. J. Geophys. Res. 106, 14,711–14,732.

Zaikowski, A., Knacke, R.F., 1975. Infrared spectra of carbonaceous chondrites and the composition of interstellar grains. Astrophys. Space Sci. 37, 3–9.

Please cite this article as: Hamilton, V.E., (2010), doi:10.1016/j.chemer.2009.12.005